

Contrasted porosity between the hanging-wall and the footwall of the active Pāpaku thrust at IODP Site U1518: insights on deformation and erosion history and sediment compaction state evolution during accretion at the northern Hikurangi margin deformation front

Dutilleul Jade¹, Bourlange Sylvain², and géraud yves¹

¹Université de Lorraine, CNRS, GeoRessources

²Université de Lorraine

November 16, 2022

Abstract

Attempts to determine physical property across thrust faults at subduction zones through drilling, logging and core sampling have been limited and restricted to exhumed accretionary prisms or shallow parts of active wedges. However, characterizing porosity evolution across the sedimentary section entering subduction zones and accreted sediments is crucial to understand deformation history at accretionary margins through determination of sediment trajectories, quantification of transported volumes of sediments and fluids with related mechanical responses and understanding deformation processes in and around fault zones. International Ocean Discovery Program Expeditions 372 and 375 drilled, logged and cored the entering basin (Site U1520) and active Pāpaku thrust (Site U1518) few kilometers landward of the northern Hikurangi margin deformation front where tsunami earthquakes and recurrent slow slip events occur. Here, we examine physical properties evolution across the Pāpaku thrust at Site U1518 including geophysical logging data, pore size distribution obtained by combining Nuclear Magnetic Resonance and Mercury Injection Capillary Pressure, and interstitial porosity that is representative of sediment compaction state, and compare with that of Site U1520. Interstitial porosity is determined by correcting total connected porosity from clay-bound water content based on cation exchange capacity. We evidence strong variations of physical properties across the thrust fault, with lower porosity, higher P-wave velocity and resistivity in the hanging-wall than in the footwall. We suggest that the porosity pattern at the Pāpaku thrust evidences differences in maximum burial depth with an overcompacted hanging-wall that has been uplifted, thrust and concomitantly eroded above a nearly normally consolidated younger footwall.

1 **Contrasted porosity between the hanging-wall and the footwall of the**
2 **active Pāpaku thrust at IODP Site U1518: insights on deformation and**
3 **erosion history and sediment compaction state evolution during**
4 **accretion at the northern Hikurangi margin deformation front**

5 Jade Dutilleul^{a*}, S. Bourlange^a and Y. Géraud^a

6 ^a*University of Lorraine, CNRS, GeoRessources, F-54000 Nancy, France*

7 *jade.dutilleul@univ-lorraine.fr

8 **Abstract**

9 Attempts to determine physical property across thrust faults at subduction zones through
10 drilling, logging and core sampling have been limited and restricted to exhumed
11 accretionary prisms or shallow parts of active wedges. However, characterizing porosity
12 evolution across the sedimentary section entering subduction zones and accreted
13 sediments is crucial to understand deformation history at accretionary margins through
14 determination of sediment trajectories, quantification of transported volumes of
15 sediments and fluids with related mechanical responses and understanding deformation
16 processes in and around fault zones. International Ocean Discovery Program
17 Expeditions 372 and 375 drilled, logged and cored the entering basin (Site U1520) and
18 active Pāpaku thrust (Site U1518) few kilometers landward of the northern Hikurangi
19 margin deformation front where tsunami earthquakes and recurrent slow slip events
20 occur. Here, we examine physical properties evolution across the Pāpaku thrust at Site
21 U1518 including geophysical logging data, pore size distribution obtained by combining
22 Nuclear Magnetic Resonance and Mercury Injection Capillary Pressure, and interstitial
23 porosity that is representative of sediment compaction state, and compare with that of
24 Site U1520. Interstitial porosity is determined by correcting total connected porosity

25 from clay-bound water content based on cation exchange capacity. We evidence strong
26 variations of physical properties across the thrust fault, with lower porosity, higher P-
27 wave velocity and resistivity in the hanging-wall than in the footwall. We suggest that
28 the porosity pattern at the Pāpaku thrust evidences differences in maximum burial depth
29 with an overcompacted hanging-wall that has been uplifted, thrust and concomitantly
30 eroded above a nearly normally consolidated younger footwall.

31 **1. Introduction**

32 Over the last two decades, strong research effort focused on better understanding how
33 the shallow part of subduction zones accommodates displacement by hosting a wide
34 variety of slip modes like tsunami earthquakes (e.g Bilek and Lay, 2002; Seno, 2002;
35 Dean et al., 2010; Geersen et al., 2013), afterslip and coseismic slip (e.g. Chlieh et al.,
36 2007), slow slip events (e.g. Liu & Rice 2007; Bell et al., 2010; Basset et al., 2014;
37 Kodaira et al., 2004; Wallace and Beavan, 2006, 2010; Song et al., 2009; Saffer and
38 Wallace, 2015; Wallace et al., 2004, 2009, 2012, 2016), steady creep (e.g. Wang and
39 Bilek, 2014), tectonic tremor (e.g. Shelly et al., 2006) and (very-)low-frequency-
40 earthquakes (e.g. Ito and Obara, 2006). Recently, IODP Expeditions 372 and 375
41 provided in situ data to investigate the physical processes thought to trigger spatial and
42 temporal transitions between fault slip styles by drilling several sites across the northern
43 Hikurangi margin, in an area offshore Gisborne where Pacific plate is obliquely
44 subducted beneath the Australian Plate at ~ 5.0 cm/y (Fig. 1a) (Wallace et al., 2004).
45 There, tsunami earthquakes nucleate (Doser and Webb, 2003) and slow slip events recur
46 down to 2km below the seafloor (Fig. 1b), potentially propagating to the trench along
47 the plate interface and/or splay faults within the prism (Saffer et al., 2019; Fagereng et
48 al., 2019; Shaddox and Schwartz, 2019; Mouslopoulou et al., 2019). Site U1520 was

49 logged and cored in the basin entering the margin ~95 km from shore and ~16 km
50 oceanward of the deformation front (Fig.1b,c) so that the initial lithological, physical,
51 hydrological and thermal properties of the input section could be characterized
52 (Dutilleul et al., in press). This site revealed a very heterogeneous input section
53 composed by a Quaternary to Paleocene sedimentary cover with siliciclastic trench
54 sediments (Units I-III) overlying pelagic carbonate formations (Unit IV), above
55 Cretaceous-aged volcanoclastic Units V-VI of the subducting Hikurangi Plateau (Barnes
56 et al., 2019; Barnes et al., 2020). Landward, in the frontal wedge ~6.5 km west of the
57 deformation front, Site U1518 penetrated an active thrust fault, the Pāpaku fault, its
58 hanging-wall and uppermost footwall up to ~492 meters below sea floor (mbsf) (Saffer
59 et al., 2019). The Pāpaku fault, intersected at ~304 mbsf, is a <math><30^\circ</math> westward-dipping
60 splay fault which is thought to lie in the SSE rupture area, to host SSEs and to have
61 accommodated several kilometers of shortening within the prism (Fagereng et al.,
62 2019). The hanging-wall corresponds to lithologic Unit I (0~304 mbsf) with Early-Mid
63 Pleistocene (>0.53 Ma) hemipelagic silty-claystone and fine-grained turbidites
64 sequences. It is folded with bedding dips ranging 0-50°, faulted and pervasively
65 fractured up to 100m above the Pāpaku fault zone (Fig. 2h). The Pāpaku thrust fault
66 zone mainly corresponds to lithologic Unit II (~304-370 mbsf; <math><0.53</math> Ma) with
67 hemipelagic mudstone alternating with thin and sparse layers of silty mudstone to sandy
68 siltstone. It is composed of a ~18m-thick main fault zone (MFZ, Fig. 2a) characterized
69 by a mixture of brittle (breccia, faults and fractures) and ductile (flow bands) structures,
70 with ductile features locally overprinted by faults and fractures (Fagereng et al., 2019).
71 Below, there are a ~21m-thick zone of gradually decreasing deformation intensity
72 where structures are more ductile than brittle, and a ~10m-thick subsidiary fault zone.
73 No significant change in lithology occurs in the footwall. It is mainly composed by

74 relatively undeformed Mid-Late Pleistocene (<0.53 Ma) Unit III (~370-492 mbsf)
75 bioturbated hemipelagic mudstones with turbidites sequences, few ductile-flow
76 deformation structures and occasional faults.

77 Here, we characterize the evolution of bound water content, pore structure and
78 interstitial porosity across the Pāpaku thrust at Site U1518. Although porosity is
79 dependent on numerous parameters like lithology, mineralogy, grain size or
80 sedimentation rates, we assume that the Quaternary siliciclastic trench sediments
81 forming the hanging-wall, the fault zone and the upper footwall at Site U1518 can be
82 correlated to undeformed Hikurangi Trough siliciclastic Units I-III at reference Site
83 U1520 (base SU4 and SU5, Fig. 1) based on seismic correlation (Barnes et al., 2020).
84 We compare interstitial porosity and pore structure data at both sites to assess how
85 accretion and thrusting affects sediment physical properties at Site U1518 and get
86 insights on deformation history at the deformation front. Following previous works
87 (Henry, 1997; Henry and Bourlange, 2004; Conin et al., 2011; Dutilleul et al., 2020 and
88 in press), we determine interstitial porosity that is representative of the compaction state
89 at Site U1518 by correcting total connected porosity (equivalent to onboard MAD
90 porosity in Wallace et al., 2019) from clay-bound water content using post-cruise
91 geochemical data like Cation Exchange Capacity (CEC) and exchangeable cation
92 composition. We further characterize the evolution of pore geometry and size with
93 increasing depth by combining Mercury Injection Capillary Pressure (MICP) and
94 Nuclear Magnetic Resonance (NMR), which yield a different range of information.

95 **2. Materials and methods**

96 ***2.1. Sampling and data***

97 Our study is based on 1) onboard data including geophysical logging data and

98 measurements on core samples and 2) post-cruise analysis of 52 core samples with
99 commonly one sample per core (approximately 1 sample each 10 meter). Samples were
100 picked up as close as possible from the samples that were squeezed onboard for
101 interstitial water composition analysis. They were shipped and stored at chilled
102 temperature (2-8°C) in sealed plastic bags with a sponge saturated with seawater to
103 preserve moisture. Comparison of onboard and post-cruise total connected porosity
104 measurement evidence that moisture was successfully preserved. Porosity data
105 measured on samples were correlated to logging-while-drilling (LWD) neutron and
106 NMR porosity data.

107 **2.2 Methods**

108 **2.2.1 Quantification of porosity**

109 **2.2.1.1. Estimation of bound water content and interstitial porosity from CEC, soluble** 110 **chloride content and interstitial water composition**

111 Total connected porosity was measured according to Blum's (1994) onboard procedure
112 that consists in measuring the mass of the sample when it's wet (m_{wet}) and it's mass
113 (m_{dry}) and volume (V_{dry} , measured using a Micromeritics® AccuPyc II 1340 helium-
114 displacement pycnometer) after a 24-hours stage of drying in a convection oven at
115 105°C±5°C to remove both interstitial and clay bound water. Interstitial water
116 corresponds to the chloride-bearing water located in the pore space that is expellable by
117 compaction-induced dewatering as sediments are buried. Clay bound water includes
118 chloride-free water located in the interlayer space and electrostatically bound on particle
119 surfaces because of the compensation of negatively charged layers by hydrated cations.
120 It is generally poorly affected by compaction (e.g. Bird 1984; Colten-Bradley, 1987;
121 Fitts and Brown, 1999; Henry and Bourlange, 2004; Dutilleul et al., 2020) and

122 transiently released when sediments reach the smectite dehydration to illite pressure-
 123 temperature (<150°C) window. The calculation of total connected porosity ϕ_t and grain
 124 density ρ_g is corrected for the precipitation of salt during drying:

$$125 \quad \phi_t = \frac{V_f}{V_{wet}} = \frac{V_f}{V_f + V_{dry} - V_{salt}} \quad \text{and} \quad \rho_g = \frac{m_s}{V_s}$$

126 where $V_f = \frac{m_f}{\rho_f}$ is the volume of pore fluid with $m_f = \frac{m_w}{1-s}$ the pore fluid mass, $m_w =$
 127 $m_{wet} - m_{dry}$ the pore water mass, s the salinity (0.035) and ρ_f the density of pore
 128 fluid (1.024 g/cm³), $V_{salt} = \frac{m_{salt}}{\rho_{salt}} = \frac{m_w s}{(1-s) \rho_{salt}}$ is the salt volume with m_{salt} the salt
 129 mass and ρ_{salt} the density of salt (2.220g/cm³), $m_s = m_{wet} - m_f = m_{dry} - m_{salt}$ is
 130 the mass of solids excluding salt and $V_s = V_{dry} - V_{salt}$ the volume of solids excluding
 131 salt.

132 Dry samples were then ground using a Retsch® mixer mill MM200 with agate grinding
 133 beads and jars. Chemical analyses including cation exchange capacity (CEC) measured
 134 by exchange with cobaltihexamine and ultraviolet-visible spectrometer Varian
 135 SpectrAA 800 Zeeman, exchangeable cation composition (Na⁺, K⁺, Ca²⁺ and Mg²⁺)
 136 measured by atomic absorption spectrometer Thermo Scientific ICE 3300 and soluble
 137 chloride content per dry mass determined by sequential water extraction (Tessier et al.,
 138 1979) and ion chromatography were carried on at the Laboratoire Interdisciplinaire des
 139 Environnements Continentaux (LIEC) in Nancy and Metz, France.

140 Interstitial porosity (ϕ_i) and bound water content (ϕ_b) were determined from the total
 141 connected porosity (ϕ_t), n the average number of water molecules per cation charge
 142 ($n=15$ is used corresponding to smectites with two layers of water following Dutilleul et
 143 al., in press and Fig. 3), M_w the water molar mass ($M_w = 0.018\text{kg/mol}$), the density of
 144 pore fluid ρ_f , the grain density ρ_g and the CEC:

$$\phi_i = \phi_t - \phi_b = \phi_t - n \frac{M_w}{\rho_f} CEC \rho_g (1 - \phi_t)$$

145 We express pore volume loss at specific depth as:

$$\frac{\Delta V}{V_o} = \frac{(\phi_{i0} - \phi_i)}{(1 - \phi_i)}$$

146 with ΔV the volume loss, V_o the initial volume and ϕ_{i0} the initial interstitial porosity

147 (Saito and Goldberg,1997)

148 **2.2.1.2. Resistivity-derived porosity**

149 We determined resistivity-derived porosity from resistivity logs at Site U1518 using

150 Revil et al. (1998)'s resistivity model for clay-rich materials with high surface

151 conductivity σ_s . This model is based on Archie's law (Archie, 1942) that links the

152 resistivity-derived porosity ϕ to the formation factor $F = a \phi^{-m}$ where m and a are

153 constants. Previous works have shown that resistivity-derived porosity determined using

154 this model with $a =1$ and a cementation factor $1 \leq m \leq 3.5$ fits interstitial porosity

155 (Conin et al., 2011; Dutilleul et al., in press) in siliciclastic clay-rich materials.

156 Assuming Bussian (1983) and Bourlange et al. (2003)'s hypotheses since $\frac{\sigma_s}{\sigma_{if}} \ll 1$ at

157 Site U1518, F can be expressed:

$$F = \frac{\sigma_{if}}{\sigma} \left[1 + 2 \frac{\sigma_s}{\sigma_{if}} \left(\frac{\sigma_{if}}{\sigma} - 1 \right) \right]$$

158 The conductivity of the interstitial fluid σ_{if} is determined from the concentration of Cl⁻,

159 Na⁺, K⁺, Ca²⁺, Mg²⁺ and SO₄²⁻ in interstitial water (C_{iws}^i) and seawater (C_{sw}^i), the ionic

160 mobility in the fluid β_f^i and Z_i the number of charges of ions given by Revil et al.

161 (1998), and σ_{sw} the sea water conductivity:

$$\sigma_{if} = \sigma_{sw} \frac{\sum_i (\beta_f^i \times Z_i \times C_{iws}^i)}{\sum_j (\beta_f^j \times Z_j \times C_{sw}^j)}$$

162 with $\sigma_{sw} = 5.32(1 + 0.02(T - 25))$ and $T(^{\circ}C) = 1.64 + 35.0 \times 10^{-3}z$ at Site
163 U1518 (Saffer et al., 2019).

164 σ_s is calculated assuming a major contribution of the Stern layer to surface electrical
165 conduction, spherical grains and a linear temperature dependency of the exchangeable
166 cation mobility β_s :

$$\sigma_s = \frac{2}{3} \rho_g CEC \beta_s$$

167 **2.2.2. Pore-network characterization**

168 Mercury Injection Capillary Pressure (MICP) and Nuclear Magnetic Resonance
169 (NMR) were performed on 14 samples to characterize macro- (>50 nm) to mesopore (2-
170 50 nm) size distribution (e.g. Dutilleul et al., in press) according to the IUPAC
171 nomenclature (Sing et al., 1985) and pore geometry evolution.

172 **2.2.2.1. Mercury Injection Capillary Pressure (MICP)**

173 MICP was performed at room temperature (20°C) using a Micromeritics® AutoPore IV
174 9500 on samples that were previously oven-dried at 105°C±5°C for 24h. The sample is
175 first degassed under vacuum during the low-pressure analysis before the volume of
176 intruded mercury is gradually measured up to a mercury pressure of ~0.2 MPa. The
177 high-pressure analysis consists in stepwise measurements of the volume of intruded
178 mercury during an intrusion-extrusion-reintrusion cycle providing the size distribution
179 of pore throats but also mercury-trapped porosity that is mercury total connected
180 porosity corrected from mercury-free porosity. During the first intrusion stage, the
181 mercury fills the connected pore space as mercury injection pressure is progressively
182 increased up to 220 MPa. This stage provides mercury-total connected porosity and the

183 distribution of the size of pore throats from 360 μm to 5.7 nm using the Young-Laplace
184 equation:

$$r = \frac{2 \sigma_{Hg} \cos \theta_{Hg}}{P_{Hg}}$$

185 where r is the pore throat radius (m), σ_{Hg} is the air-mercury interfacial tension (0.485
186 N/m), θ_{Hg} is the mercury-sediment contact angle (140°) and P_{Hg} is the mercury
187 injection pressure (Pa). During the extrusion stage, the pressure is decreased down to
188 atmospheric pressure with some mercury droplets remaining trapped at narrow pore
189 throats (Li and Wardlaw, 1986a, b) allowing to determine the mercury-trapped porosity,
190 an indicator of pore compaction state. Finally, mercury-free porosity only is reintruded
191 as mercury injection pressure is increased up to the maximum value of 220 MPa. The
192 distribution of pore throats size was used to determine permeability K_{KT} using the Katz-
193 Thompson permeability model (Katz and Thompson, 1986,1987; Nishiyama and
194 Yokoyama, 2014):

$$195 \quad K_{KT} = \frac{1}{89} \phi_i \frac{(l_{max}^h)^3}{l_c} f(l_{max}^h)$$

196 with l_c the pore throat diameter of the inflexion point of the cumulative pore-throat size
197 distribution, l_{max}^h the pore throat diameter corresponding to the optimum path for
198 permeability where the fractional volume of pore diameters of l and larger $f(l_{max}^h)$ is
199 maximum.

200 **2.2.2.2. Nuclear Magnetic Resonance (NMR)**

201 NMR measurements were performed using Bruker® Minispec Mq20 at room
202 temperature (20°C) and atmospheric pressure on core samples with a diameter of 8 mm.
203 The transverse relaxation time T_2 was measured using the Carr-Purcell-Meilboom-Gill
204 (CPMG) sequence with a recycle delay of 0.1s and a half-echo time τ of 0.04 ms (the

205 minimum available for this equipment), a gain ranging 70-80%, 200 echoes per scan
206 and 128 scans were stacked. We used UpenWin© software to inverse the raw T_2
207 exponential decay in a smoothed T_2 distribution. We correlated the T_2 (msec) measured
208 to MICP pore throat radius (μm) based on ρ_e the effective relaxivity ($\mu\text{m}/\text{sec}$) following
209 Marschall et al. (1995) using the relation:

$$T_2 = \frac{1000r}{2\rho_e}$$

210 We also determined NMR porosity as suggested by Daigle et al. (2014) based on the
211 volume of water V_w in the sample:

$$\phi_{NMR} = \frac{V_w}{V_w + V_s}$$

212 V_w is determined using a calibration where the maximum signal amplitude A_0 (corrected
213 for the gain) is recorded during the T_2 measurement for known volume of water:
214 $V_w = 19.762A_0 - 0.092$ ($R^2 = 0.94$). This method was validated using synthetic samples of
215 known porosity.

216 **3. Results**

217 **3.1. Mineralogy and Cation Exchange Capacity (CEC)**

218 Total clay content is relatively homogeneous and elevated (32%-52%, in
219 average ~46%) through Unit I to III with no change from either side of the fault zone
220 (Fig. 2b). Cation exchange capacity is low to intermediate (0.08-0.18 mol/kg, in average
221 0.15 mol/kg) through the sedimentary section (Fig. 2c). CEC tends to increase with total
222 clay content and shows minimum values in Subunit IIIA contorted domains possibly
223 corresponding to mass transport deposits (MTDs). This range of CEC values suggests
224 that the clay mineral assemblage is mainly composed of kaolinite and/or chlorite and/or
225 illite rather than smectite.

226

3.2. *Physical properties*

227 Overall, onboard total connected porosity averages 43% at Site U1518 but exhibits a
228 large scatter up to 11%. There is a remarkable total connected porosity difference >10%
229 between the hanging-wall and the footwall, with a hanging-wall exhibiting a general
230 trend of lower values compared to the footwall. In both the hanging-wall and the
231 footwall, total connected porosity decreases exponentially with increasing depth z or
232 effective vertical stress σ'_v with similar Archie's law parameters (Table 1). In the
233 hanging-wall, total connected porosity exponentially decreases from ~66% near the
234 seafloor to ~40% at bottom of the Pāpaku main fault zone (Fig. 2d), with Subunit IB
235 showing values that are a few percent higher and that decrease more quickly with
236 increasing depth than in Subunit IA. Across the Pāpaku fault zone, total connected
237 porosity increases up to 54% with wide and reduced scatter in the main and subsidiary
238 fault zones respectively. In the footwall, total connected porosity decreases to 39%, with
239 slightly higher values in Subunit IIIB than IIIA. Although a major transition in porosity
240 occurs at the fault zone, it is possible to fit a single Archie's law across the Pāpaku
241 thrust that is $\phi_t = 44.3e^{-\frac{z}{12937}}$ or $\phi_t = 44.3e^{-0.012\sigma'_v}$.

242 As a result of relatively constant and low CEC values, bound water content is constant
243 and low (3-8%, in average 6%) across the section drilled at Site U1518 (Fig. 2d).

244 Because of relatively constant bound water content, the evolution of interstitial porosity
245 (Fig. 2d and g) is very similar to that of total connected porosity, showing a ~10%
246 increase through the Pāpaku fault zone and comparable exponential decrease trends
247 with increasing depth in the footwall and the hanging-wall (Table 1). Interstitial
248 porosity decreases in the hanging-wall from 62% to ~33% at the top of the fault zone
249 with a few percent higher values in Subunit IB than IA, increases up to 48% through the
250 fault zone and decreases up to ~33% through the footwall with slightly higher values in

251 Subunit IIIB than IIIA. Resulting total pore volume loss (Saito and Goldberg, 1997) is
252 twice higher in the hanging-wall (~0.4) than in the footwall (~0.2).

253 LWD neutron and NMR porosities (Wallace et al., 2019) show a global trend that
254 matches that of total connected and interstitial porosities, with exacerbated porosity
255 contrast between the hanging-wall and the footwall (Fig. 2d). Continuous LWD porosity
256 data are able to record detailed porosity evolution across the Pāpaku fault zone. Both
257 LWD neutron and NMR porosity increase by stages through the main fault zone, the
258 subsidiary fault zone and the zone in between. Overall, LWD neutron porosity
259 satisfying fits to total connected porosity but exhibits higher porosity difference
260 between the hanging-wall and the footwall with values up to 5% higher than measured
261 on samples in the footwall. LWD NMR porosity values are significantly lower than
262 interstitial and total connected porosities, except in Subunit IA where it fits interstitial
263 porosity. It exhibits the highest porosity shift (~20%) through the Pāpaku fault zone.

264 Resistivity-derived porosity can be fitted to interstitial porosity data using $m = 2.2$ in
265 Subunit IA and $m = 2.7$ from Subunit IB to IIIB. The shift toward higher cementation
266 factor values occurs at the coring gap in the hanging-wall that also corresponds to the
267 top of the hanging-wall damage zone.

268 Overall, LWD resistivity and P-wave velocity are anti-correlated with porosity (Fig. 2f).
269 P-wave velocity (resp. resistivity) increases from ~1550 m/s (resp. ~1.8 ohm/m) at the
270 seafloor to ~2200m/s (resp. ~3.8 ohm/m) at the bottom of the hanging-wall, decreases to
271 ~1700 m/s (resp. ~1.5 ohm/m) across the Pāpaku fault zone and increases up to ~2100
272 m/s (resp. ~2.4 ohm/m) in the footwall. Within the Pāpaku fault zone, both P-wave
273 velocity and resistivity decrease by stages in the main fault zone, the subsidiary fault
274 zone and in between.

275

3.3 Pore structure

276 Overall, MICP and NMR (Fig. 2e) show that samples are macroporous (i.e. pore
277 diameters >50 nm using the nomenclature of Sing et al., 1985) with only one family of
278 pore size that globally decreases and becomes more homogeneous with increasing
279 depth, from ~ 0.8 μm in average near the seafloor to ~ 0.2 μm in average in Subunit IIIB,
280 except in the Pāpaku fault zone where it locally increases and becomes more
281 heterogeneous. A slight increase in pore size can also be noticed in Subunit IIIB
282 compared to Subunit IIIA.

283 At Site U1518, there is no clear relation between interstitial porosity and mean pore
284 throats diameter, mercury porosity or mercury trapped porosity for the hanging-wall, the
285 fault zone and the footwall (Fig. 4). Katz-Thompson permeability decreases with depth
286 from $\sim 7.25 \cdot 10^{-17}$ m^2 to $\sim 1.3 \cdot 10^{-17}$ m^2 in the hanging-wall, ranges $1.2 \cdot 10^{-17}$ - $6.3 \cdot 10^{-18}$ m^2 in
287 the Pāpaku fault zone and $1.05 \cdot 10^{-16}$ - $3.6 \cdot 10^{-17}$ m^2 in the footwall.

288 Average NMR T_2 signals follow the same evolution than pore throats size given by
289 MICP, although strong discrepancy occurs between the values measured by the LWD
290 tool and on the samples. T_2 measured on the samples is ~ 2.8 ms near the seafloor and
291 decreases to ~ 2 ms in the footwall. LWD NMR T_2 steadily decreases from ~ 9 ms near
292 the seafloor to ~ 4 ms at the bottom of the hanging-wall, increases through the Pāpaku
293 fault zone up to 25 ms, and steadily decreases through the footwall to ~ 7 ms. This
294 discrepancy could be due to a different calibration of the LWD NMR tool (Wallace et
295 al., 2019) compared to laboratory measuring device.

296 **4. Discussion**

297 **4.1. Comparison of interstitial porosity and pore structure data of accreted**
298 **Quaternary siliciclastic sequence at Site U1518 with undeformed sequence at**
299 **Site U1520**

300 Porosity data in accreted siliciclastic Quaternary sequence at Site U1518 including
301 interstitial porosity data that is representative of the compaction state exhibit contrasted
302 values in the hanging-wall and the footwall of the Pāpaku thrust. If the hanging-wall
303 and the footwall show interstitial porosity values that similarly exponentially decrease
304 with increasing depth (Fig. 2d, g) or effective vertical stress (Table 1), the hanging-wall
305 is characterized by lower values than the footwall, the transition to higher porosity
306 values occurring across the Pāpaku fault zone.

307 This evolution of interstitial porosity at Site U1518 contrasts with that of the correlated
308 undeformed sequence drilled seaward at Site U1520 (Fig. 1c), that exclusively shows
309 exponential decrease with increasing effective vertical stress following the reference
310 compaction curve $\phi_i = 46.6e^{-0.029 \sigma'_v}$ ($R^2=0.29$) from ~66% near the seafloor to 40% at
311 the bottom of siliciclastic Unit III (Fig. 5). This compaction trend is attributed to normal
312 consolidation associated with pre-accretion compaction-induced dewatering that
313 releases interstitial water as the sequence is progressively buried in the basin entering
314 the subduction zone (Bray and Karig, 1985). By comparison, interstitial porosity is
315 more scattered at Site U1518 than at Site U1520. In average, it is ~5-10% lower in the
316 hanging-wall at Site U1518 than the reference U1520 compaction curve at this range of
317 depth. Through the Pāpaku fault zone, interstitial porosity increases up to a range of
318 values close to U1520 compaction curve values at these depths. In the upper section of
319 the footwall drilled at Site U1518, it nearly averages the values of the reference curve or
320 is only few percent lower. The comparison of interstitial porosity data in accreted

321 siliciclastic Quaternary sequence at Site U1518 with the reference compaction curve
322 determined from correlated undeformed sequence at Site U1520 evidences an
323 overcompacted hanging-wall as mentioned by Fagereng et al. (2019), a normally
324 consolidated Pāpaku fault zone and a slightly overcompacted to nearly normally
325 consolidated upper footwall at Site U1518 (Fig. 5a).

326 Pore diameter measured by MICP and estimated from NMR measurements on samples
327 and LWD NMR is equivalent at Site U1518 and in Site U1520 siliciclastic units (Fig.
328 6a), except in the intensively fractured part the hanging-wall >100 mbsf at Site U1518
329 where it is lower (~0.2 μm) than at equivalent depth at Site U1520 where it averages 0.5
330 μm (Fig. 6b). T_2 measured on samples and LWD T_2 show similar behaviour (Fig. 6c).
331 Katz-Thompson permeability is also ~1 order of magnitude lower in the hanging-wall at
332 Site U1518 than at equivalent depth at Site U1520 (Fig. 6d). Globally, the trends
333 relating interstitial porosity, mean pore throats diameters, mercury porosity and mercury
334 trapped porosity in undeformed siliciclastic sediments at Site U1520 is suitable for
335 sediments at Site U1518, although these latter mostly correspond to a low porosity-
336 small pores endmember (Fig. 4).

337 *4.2. Insights on compaction state evolution and deformation history of* 338 *Quaternary siliciclastic sequence during accretion*

339 Progressive burial of unconsolidated sediments deposited in the basin entering
340 subduction zones results in the mechanical compaction of the pore network with
341 continuous release of interstitial water until lithification into rocks (e.g. Bray and Karig,
342 1985; Fagereng et al., 2018). In drained conditions, compaction-induced dewatering is
343 thus associated with a reduction and homogenization of pore diameters, an exponential
344 decrease of interstitial porosity (vertical loading trend following the normal

345 consolidation curve $\phi_i = ae^{-b\sigma'_v}$, Fig. 7) and possibly a reduction of permeability.
346 Tectonic and hydrologic events that commonly occurs in the shallow part of subduction
347 zones deviates interstitial porosity from the normal consolidation trend (Bray and Karig,
348 1985 and references therein; Saito and Goldberg, 1997; Conin et al., 2011) as detailed in
349 Figure 7.

350 Based on these theoretical shifts, we propose a simple model where erosion and
351 thrusting are concomitant and potentially associated with excess pore pressure build up
352 and horizontal shortening to explain the interstitial porosity profile observed at Site
353 U1518 (Fig. 8). In the hanging-wall, the interstitial porosity data are significantly lower
354 than the value of the reference compaction curve and can be fitted to the latter assuming
355 a vertical effective stress increase of $\sim 7.5 \pm 1.0$ MPa corresponding to $\sim 830 \pm 110$ meters
356 of supplementary burial occurred (Fig. 5b). In the footwall where the data are closer to
357 the reference compaction curve, a lower vertical effective stress increase of $\sim 3.0 \pm 1.0$
358 MPa corresponding to $\sim 330 \pm 110$ meters of supplementary burial has to be assumed.
359 Such stress shifts could be the result of erosion (Fig. 7b).

360 We suggest that both the hanging-wall and the footwall sequences have experienced
361 vertical loading as they were progressively buried after deposition in the entering basin,
362 resulting in decreasing pore size with increasing depth and in the normal consolidation
363 trends observed (Fig. 7a; 8a). The trends for the hanging-wall and footwall (Table 1) are
364 similar because of analogous lithology in both sequences. Based on stress shift values,
365 we infer that the sequence that will later form the hanging-wall was buried $\sim 830 \pm 110$
366 meters deeper than present depth in the entering basin before thrust, thus reaching a
367 maximum thickness of $\sim 1130 \pm 110$ meters. This estimation is in accordance with the
368 depth at the trench of the base SU4 reflector (Fig. 1c) that approximately corresponds to
369 the base of the hanging-wall at Site U1518. This suggests that the tectonic setting at Site

370 U1518 before thrust is analogous to present tectonic setting at the trench. This
371 significant thickness is likely to have favoured sediment consolidation and transition to
372 brittle behaviour with faults and fractures development. We explain the stress shift for
373 the footwall showing that the latter was buried $\sim 330 \pm 110$ meters deeper than present
374 depth by erosion history occurring in at least two main stages in a case of limit scenario.
375 In a first time, ~ 500 meters of the hanging-wall sequence was eroded as it was thrust
376 above the footwall (Fig. 8b). In a second time, once the hanging-wall was set above the
377 footwall for a maximum thickness of $\sim 630 \pm 110$ meters, $\sim 330 \pm 110$ meters of material
378 was eroded so the hanging-wall reaches its actual thickness of ~ 300 meters (Fig. 8c).
379 These values represent maximum values assuming perfectly drained conditions and no
380 overcompaction associated with tectonic strain (Fig. 7c). However, it is very likely that
381 these values are overestimated because 1) the hanging-wall may have undergone
382 horizontal shortening as it was folded and thrust (e.g. Saffer and Tobin, 2011;
383 Hamahashi et al., 2013) and 2) conditions may not have been perfectly drained in the
384 footwall allowing to pore pressure build-up as the hanging-wall was thrust above it
385 (Fig. 7d). Elevated pore fluid pressure in the footwall is suggested by the injection
386 features observed in intervals showing ductile flow structures (Fagereng et al., 2019).
387 Because of the lower peak P-T conditions experienced by the footwall compared to the
388 hanging-wall, the footwall was likely weaker than the hanging-wall during faulting
389 (Hamashi et al., 2013) and composed by poorly consolidated fluid-rich sediments where
390 excess pore pressure may have developed as a response to the thrusting of the hanging-
391 wall above it. Present interstitial porosity profile in the footwall implies that
392 overpressured fluids were expelled before the second erosion stage, allowing the poorly
393 deformed footwall to consolidate and to develop few brittle deformation structures.

394 *4.3 Comparison with other splay faults*

395 Although limited in situ geophysical or core data are available in clay-rich thrust faults,
396 similar porosity contrasts between the footwall and the hanging-wall have been
397 observed at exhumed (e.g. Hamahashi et al., 2013) and modern splay faults (e.g. Saito
398 and Goldberg, 1997 at Barbados; Bourlange et al., 2003; Conin et al., 2011; Tao and
399 Sen, 2012; Cerchiari et al., 2018 at Nankai), with also higher porosity in the footwall
400 than in the hanging-wall. Overall, this porosity transition across the fault zone evidences
401 difference in maximum burial depth, with uplifted and unroofed overcompacted
402 hanging-wall above younger less consolidated footwall. Overcompaction of the
403 hanging-wall may also be favoured by the thickening of the prism as thrust sheets stack,
404 resulting in horizontal shortening and tectonic compaction (Saito and Goldberg, 1997).
405 Here, similarly to Conin et al. (2011) and Hamahashi et al. (2013) but contrary to Saito
406 and Goldberg (1997) a unique cementation factor m is required to fit the porosity data
407 across the damage zone of the hanging-wall, the fault zone and the footwall. At the
408 Pāpaku thrust, m is higher but in the range of values that has been previously described
409 at modern splay faults of the Nankai Kumano transect (Conin et al., 2011) or Barbados
410 (Saito and Goldberg, 1997) although the quantitative method used in the latter study is
411 not rigorously based on the same hypotheses. In particular, the lower m value found in
412 the poorly damaged part of the hanging-wall that roughly corresponds to Subunit IA
413 contrasts with the work of Saito and Goldberg (1997) that evidences higher m in the
414 hanging-wall than in the footwall, although a varies. However, it contrasts with the very
415 low values evidenced at exhumed splay faults where porosity decreases (Hamahashi et
416 al., 2013). The unique value of m for the deformed hanging-wall, the fault zone and the
417 footwall may be related to similarities in microstructures and mineralogy in the footwall
418 and the hanging-wall (e.g. Hamahashi et al., 2013) although grain size slightly differs
419 between both.

420 **5. Conclusion**

421 Based on IODP Expeditions 372/375 logging data and samples, we have evidenced
422 strong porosity contrasts between the hanging-wall and the footwall of the active
423 Pāpaku splay fault at northern Hikurangi margin. As observed at exhumed and modern
424 splay faults at different subduction zones, the footwall is characterized by higher
425 porosity values than the hanging-wall that is overconsolidated compared to equivalent
426 normally consolidated siliciclastic input sequence at Site U1520. Resistivity and P-wave
427 velocity exhibit an evolution that is anti-correlated with that of porosity. Based on
428 porosity reversals from the reference compaction curve at Site U1520, we suggest that
429 the hanging-wall underwent pre-accretion consolidation as it was buried in the entering
430 basin in a setting that is similar to that of the actual proto-thrust, before being thrust
431 above younger and less consolidated sediments of the footwall and unroofed by
432 concomitant erosion. Other processes may have contributed to shift porosity from the
433 reference compaction curve like 1) the build-up of pore pressure in the footwall in case
434 of disequilibrium compaction and 2) poorly drained conditions and folding and
435 thrusting of the hanging-wall associated with horizontal shortening. Overall, the Pāpaku
436 thrust at northern Hikurangi margin exhibits lithological, structural and physical
437 properties similar to that of shallow splay faults in early stage of deformation, although
438 present data do not allow to precisely quantify dewatering and pore pressure.

439 **6. Acknowledgements**

440 We greatly acknowledge the funding of the shore-based measurements of CNRS-INSU
441 and IODP-France. We thank David Billet, Philippe Rousselle, Maximilien Beuret,
442 Géraldine Kitzinger and Hervé Marmier from the LIEC laboratory in Nancy and Metz
443 (France) for running CEC, exchangeable cation composition and soluble chloride
444 content analyses.

445 **7. Data**

446 This research used data provided by the International Ocean Discovery Program (IODP)
447 and freely available on the LIMS Report Interface Page at web.iodp.tamu.edu/LORE or
448 on the log database at mlp.ldeo.columbia.edu/logdb/scientific_ocean_drilling. Post-
449 cruise data including corrected porosity, CEC, exchangeable cation composition, MICP
450 and NMR are available in the OTELO Research Data Repository
451 (<https://doi.org/10.24396/ORDAR-31>).

452 **8. References**

453 Archie, G. E. (1942). The electrical resistivity log as an aid in determining some
454 reservoir characteristics, *Trans. Am. Inst. Min. Metall. Pet. Eng.*, 146, 54-62

455 Barnes, P.M., Wallace, L.M., Saffer, D.M., Pecher, I.A., Petronotis, K.E., LeVay, L.J.,
456 Bell, R.E., Crundwell, M.P., Engelmann de Oliveira, C.H., Fagereng, A., Fulton, P.M.,
457 Greve, A., Harris, R.N., Hashimoto, Y., Hüpers, A., Ikari, M.J., Ito, Y., Kitajima, H.,
458 Kutterolf, S., Lee, H., Li, X., Luo, M., Malie, P.R., Meneghini, F., Morgan, J.K., Noda,
459 A., Rabinowitz, H.S., Savage, H.M., Shepherd, C.L., Shreedharan, S., Solomon, E.A.,
460 Underwood, M.B., Wang, M., Woodhouse, A.D., Bourlange, S.M., Brunet, M.M.Y.,
461 Cardona, S., Clennell, M.B., Cook, A.E., Dugan, B., Elger, J., Gamboa, D.,
462 Georgiopoulou, A., Han, S., Heeschen, K.U., Hu, G., Kim, G.Y., Koge, H., Machado,
463 K.S., McNamara, D.D., Moore, G.F., Mountjoy, J.J., Nole, M.A., Owari, S., Paganoni,
464 M., Rose, P.S., Sreaton, E.J., Shankar, U., Torres, M.E., Wang, X., and Wu, H.-Y.
465 (2019). Site U1520. In Wallace, L.M., Saffer, D.M., Barnes, P.M., Pecher, I.A.,
466 Petronotis, K.E., LeVay, L.J., and the Expedition 372/375 Scientists, Hikurangi
467 Subduction Margin Coring, Logging, and Observatories. (2019). Proceedings of the

468 International Ocean Discovery Program, 372B/375: College Station, TX (International
469 Ocean Discovery Program). <https://doi.org/10.14379/iodp.proc.372B375.105.2019>

470 Barnes, P.M., Wallace, L.M., Saffer, D.M., Bell, R.E., Underwood, M.B., Fagereng, A.,
471 Meneghini, F., Savage, H.M., Rabinowitz, H.S., Morgan, J.K., et al. (2020). Slow slip
472 source characterized by lithological and geometric heterogeneity. *Science Advances* 6,
473 eaay3314.

474 Bassett, D., Sutherland, R., and Henrys, S. (2014). Slow wavespeeds and fluid
475 overpressure in a region of shallow geodetic locking and slow slip, Hikurangi
476 subduction margin, New Zealand. *Earth and Planetary Science Letters* 389, 1–13.

477 Bell R, Sutherland R, Barker DHN, Henrys S, Bannister S, et al. (2010). Seismic
478 reflection character of the Hikurangi subduction interface, New Zealand, in the region
479 of repeated Gisborne slow slip events. *Geophys. J. Int.* 180(1):34–48

480 Bilek, S.L., and Lay, T. (2002). Tsunami earthquakes possibly widespread
481 manifestations of frictional conditional stability: Variability of Greenland accumulation.
482 *Geophysical Research Letters* 29, 18-1-18–4.

483 Bird, P. (1984). Laramide crustal thickening event in the Rocky Mountain Foreland and
484 Great Plains: *Tectonics*, v. 3, no. 7, p. 741–758, doi:10.1029/TC003i007p00741.

485 Blum, P. (1994). Index properties, vers. 155. In ODP Shipboard laboratory Manual,
486 College Station, TX (Ocean drilling Program).

487 Bourlange, S., Henry, P., Moore, J.C., Mikada, H., Klaus, A. (2003). Fracture porosity
488 in the décollement zone of Nankai accretionary wedge using Logging while Drilling
489 resistivity data. *Earth Planet. Sci. Lett.* 209, 103–112. [https://doi.org/10.1016/S0012-](https://doi.org/10.1016/S0012-821X(03)00082-7)
490 [821X\(03\)00082-7](https://doi.org/10.1016/S0012-821X(03)00082-7).

491 Bray, C. J. and Karig, D. E. (1985). Porosity of sediments in accretionary prisms and
492 some implications for dewatering processes, *J. Geophys. Res.*, 90, 768–778,
493 <https://doi.org/10.1029/JB090iB01p00768>

494 Bussian, A.E., (1983). Electrical conductance in a porous medium. *Geophysics* 48 (9),
495 1258–1268. <https://doi.org/10.1190/1.1441549>.

496 Cerchiari, A., Fukuchi, R., Gao, B., Hsiung, K.-H., Jaeger, D., Kaneki, S., Keller, J.,
497 Kimura, G., Kuo, S.-T., Lymer, G., et al. (2018). IODP workshop: Core-Log Seismic
498 Investigation at Sea – Integrating legacy data to address outstanding research questions
499 in the Nankai Trough Seismogenic Zone Experiment. *Scientific Drilling* 24, 93–107.

500 Chlieh, M., Avouac, J.-P., Hjorleifsdottir, V., Song, T.-R.A., Ji, C., Sieh, K., Sladen, A.,
501 Hebert, H., Prawirodirdjo, L., Bock, Y., et al. (2007). Coseismic Slip and Afterslip of
502 the Great Mw 9.15 Sumatra-Andaman Earthquake of 2004. *Bulletin of the*
503 *Seismological Society of America* 97, S152–S173.

504 Conin, M., Henry, P., Bourlange, S., Raimbourg, H., and Reuschlé, T. (2011).
505 Interpretation of porosity and LWD resistivity from the Nankai accretionary wedge in
506 light of clay physicochemical properties: Evidence for erosion and local overpressuring:
507 Porosity and LWD resistivity from Nankai. *Geochemistry, Geophysics, Geosystems* 12.

508 Colten-Bradley, V.A. (1987). Role of pressure in smectite dehydration - effects on
509 geopressure and smectite-to-illite transformation, *AAPG Bull.* 71, 1414-1427.

510 Daigle, H., Thomas, B., Rowe, H., and Nieto, M. (2014). Nuclear magnetic resonance
511 characterization of shallow marine sediments from the Nankai Trough, Integrated
512 Ocean Drilling Program Expedition 333: NMR of Nankai Trough sediments. *Journal of*
513 *Geophysical Research: Solid Earth* 119, 2631–2650.

514 Dean, S.M., McNeill, L.C., Henstock, T.J., Bull, J.M., Gulick, S.P.S., Austin, J.A.,
515 Bangs, N.L.B., Djajadihardja, Y.S., and Permana, H. (2010). Contrasting Décollement
516 and Prism Properties over the Sumatra 2004-2005 Earthquake Rupture Boundary.
517 *Science* 329, 207–210.

518 Doser, D.I., and Webb, T.H. (2003). Source parameters of large historical (1917-1961)
519 earthquakes, North Island, New Zealand. *Geophysical Journal International* 152, 795–
520 832.

521 Dutilleul, J., Bourlange, S., Conin, M., and Géraud, Y. (2020). Quantification of bound
522 water content, interstitial porosity and fracture porosity in the sediments entering the
523 North Sumatra subduction zone from Cation Exchange Capacity and IODP Expedition
524 362 resistivity data. *Marine and Petroleum Geology* 111, 156–165.

525 Fagereng, Å, Diener, J.F.A., Ellis, S., and Remitti, F. (2018). Fluid-related deformation
526 processes at the up- and downdip limits of the subduction thrust seismogenic zone:
527 What do the rocks tell us?, in Byrne, T., Underwood, M.B., Fisher, D., McNeill, L.,
528 Saffer, D., Ujiie, K., and Yamaguchi, A., eds., *Geology and Tectonics of Subduction*
529 *Zones: A Tribute to Gaku Kimura: Geological Society of America Special Paper* 534, p.
530 187–215, [https://doi.org/10.1130/2018.2534\(12\)](https://doi.org/10.1130/2018.2534(12)).

531 Fagereng, Å., Savage, H.M., Morgan, J.K., Wang, M., Meneghini, F., Barnes, P.M.,
532 Bell, R., Kitajima, H., McNamara, D.D., Saffer, D.M., et al. (2019). Mixed deformation
533 styles observed on a shallow subduction thrust, Hikurangi margin, New Zealand. *47*, 6.

534 Fitts, T.G. and Brown, K.M. (1999). Stress-induced smectite dehydration: ramifications
535 for patterns of freshening and fluid expulsion in the N. Barbados accretionary wedge,
536 *Earth Planet. Sci. Lett.* 172, 179-197.

537 Geersen, J., McNeill, L., Henstock, T.J., and Gaedicke, C. (2013). The 2004 Aceh-
538 Andaman Earthquake: Early clay dehydration controls shallow seismic rupture: Shallow
539 Rupture off Northern Sumatra. *Geochemistry, Geophysics, Geosystems* 14, 3315–3323.

540 Hamahashi, M., Saito, S., Kimura, G., Yamaguchi, A., Fukuchi, R., Kameda, J.,
541 Hamada, Y., Kitamura, Y., Fujimoto, K., Hashimoto, Y., et al. (2013). Contrasts in
542 physical properties between the hanging wall and footwall of an exhumed seismogenic
543 megasplay fault in a subduction zone-An example from the Nobeoka Thrust Drilling
544 Project: physical property of exhumed splay fault. *Geochemistry, Geophysics,*
545 *Geosystems* 14, 5354–5370.

546 Henry, P. (1997). Relationship between porosity, electrical conductivity and cation
547 exchange capacity in Barbados wedge sediments, *Proc. Ocean Drill. Program Sci.*
548 *Results*, 156, 137–149

549 Henry, P., Bourlange, S., (2004). Smectite and fluid budget at Nankai IODP sites
550 derived from cation exchange capacity. *Earth Planet. Sci. Lett.* 219, 129–145.
551 [https://doi.org/10.1016/S0012-821X\(03\)00694-0](https://doi.org/10.1016/S0012-821X(03)00694-0).

552 Ito, Y., Obara, K. (2006). Very low frequency earthquakes within accretionary prisms
553 are very low stress-drop earthquakes. *Geophys. Res. Lett.* 33:L09302

554 Katz, A.J., and Thompson, A.H. (1986). Quantitative prediction of permeability in
555 porous rock. *Physical Review B* 34, 8179–8181.

556 Katz, A.J., and Thompson, A.H. (1987). Prediction of rock electrical conductivity from
557 mercury injection measurements. *Journal of Geophysical Research* 92, 599.

558 Kodaira, S., Iidaka, T., Kato, A., Park, J.-O., Iwasaki, T., and Kaneda, Y. (2004) High
559 pore fluid pressure may cause silent slip in the Nankai Trough: *Science*, v. 304, p.
560 1295–1298, <https://doi.org/10.1126/science.1096535>.

561 Li, Y. and N.C., Wardlaw (1986a). The influence of wettability and critical pore throat
562 size ratio on snap-off, *Journal of Colloid and Interface Science*, 109(2), 461-472

563 Li, Y. and N.C., Wardlaw (1986b). Mechanisms of nonwetting phase trapping during
564 imbibition at slow rates, *Journal of Colloid and Interface Science*, 109(2), 473-486

565 Liu, Y., and Rice, J.R. (2007). Spontaneous and triggered aseismic deformation
566 transients in a subduction fault model. *Journal of Geophysical Research* 112.

567 Marschall, D., Gardner, J.S., Mardon, D., and Coates, R. (1995). Method for Correlating
568 NMR Relaxometry and Mercury injection Data. 12.

569 Mouslopoulou, V., Saltogianni, V., Nicol, A., Oncken, O., Begg, J., Babeyko, A.,
570 Cesca, S., and Moreno, M. (2019). Breaking a subduction-termination from top to
571 bottom: The large 2016 Kaikōura Earthquake, New Zealand. *Earth and Planetary*
572 *Science Letters* 506, 221–230.

573 Nishiyama, N., and Yokoyama, T. (2014). Estimation of permeability of sedimentary
574 rocks by applying water-expulsion porosimetry to Katz and Thompson model.
575 *Engineering Geology* 177, 75–82.

576 Revil, A., Cathles III, L. M., Losh, S. and Nunn, J. A. (1998). Electrical conductivity in
577 shaly sands with geophysical applications, *J. Geophys. Res.*, 103, 23,925–23,936,
578 doi:10.1029/98JB02125.

579 Saffer, D.M., and Tobin, H.J. (2011). Hydrogeology and Mechanics of Subduction Zone
580 Forearcs: Fluid Flow and Pore Pressure. *Annual Review of Earth and Planetary*
581 *Sciences* 39, 157–186.

582 Saffer, D.M., and Wallace, L.M. (2015). The frictional, hydrologic, metamorphic and
583 thermal habitat of shallow slow earthquakes: *Nature Geoscience*, v. 8, p. 594–600,
584 <https://doi.org/10.1038/ngeo2490>.

585 Saffer, D.M., Wallace, L.M., Barnes, P.M., Pecher, I.A., Petronotis, K.E., LeVay, L.J.,
586 Bell, R.E., Crundwell, M.P., Engelmann de Oliveira, C.H., Fagereng, A., Fulton, P.M.,
587 Greve, A., Harris, R.N., Hashimoto, Y., Hüpers, A., Ikari, M.J., Ito, Y., Kitajima, H.,
588 Kutterolf, S., Lee, H., Li, X., Luo, M., Malie, P.R., Meneghini, F., Morgan, J.K., Noda,
589 A., Rabinowitz, H.S., Savage, H.M., Shepherd, C.L., Shreedharan, S., Solomon, E.A.,
590 Underwood, M.B., Wang, M., Woodhouse, A.D., Bourlange, S.M., Brunet, M.M.Y.,
591 Cardona, S., Clennell, M.B., Cook, A.E., Dugan, B., Elger, J., Gamboa, D.,
592 Georgiopoulou, A., Han, S., Heeschen, K.U., Hu, G., Kim, G.Y., Koge, H., Machado,
593 K.S., McNamara, D.D., Moore, G.F., Mountjoy, J.J., Nole, M.A., Owari, S., Paganoni,
594 M., Rose, P.S., Screatton, E.J., Shankar, U., Torres, M.E., Wang, X., and Wu, H.-Y.
595 (2019). Expedition 372B/375 summary. In Wallace, L.M., Saffer, D.M., Barnes, P.M.,
596 Pecher, I.A., Petronotis, K.E., LeVay, L.J., and the Expedition 372/375 Scientists,
597 Hikurangi Subduction Margin Coring, Logging, and Observatories. Proceedings of the
598 International Ocean Discovery Program, 372B/375: College Station, TX (International
599 Ocean Discovery Program). <https://doi.org/10.14379/iodp.proc.372B375.101.2019>

600 Shaddock, H.R., and Schwartz, S.Y. (2019). Subducted seamount diverts shallow slow
601 slip to the forearc of the northern Hikurangi subduction zone, New Zealand. *Geology*
602 47, 415–418.

603 Saito, S., and Goldberg, D. (1997). Evolution of tectonic compaction in the Barbados
604 accretionary prism: Estimates from logging-while-drilling. *Earth and Planetary Science*
605 *Letters* 148, 423–432.

606 Shelly, D. R., Beroza, G.C., Iden S., Nakamura, S. (2006). Low frequency earthquakes
607 in Shikoku, Japan, and their relationship to episodic tremor and slip. *Nature* 442:188–91

608 Seno, T. (2002). Tsunami earthquakes as transient phenomena. *Geophysical Research*
609 *Letters* 29, 58-1-58–4.

610 Sing, K.S., Everett, D.H., Haul, R.A.W., Moscou, L., Pierotti, R.A., Rouquerol, J.,
611 Siemieniewsha, T., (1985). Reporting physisorption data for gas/solid systems with
612 special reference to the determination of surface area and porosity. *Pure Appl. Chem.*
613 57, 603e619.

614 Song, T.A., Helmberger, D.V., Brudzinski, M.R., Clayton, R.W., Davis, P., et al.
615 (2009). Subducting slab ultra-slow velocity layer coincident with silent earthquakes in
616 southern Mexico. *Science* 324:502–6

617 Tao, Y., and Sen, M.K. (2012). Shallow splay fault properties of the Nankai Trough
618 accretionary wedge inferred from seismic inversion. *Journal of Geophysics and Engineering*
619 9, 1–11.

620 Wallace, L.M., Beavan, J., McCaffrey, R., and Desmond, D. (2004). Subduction zone
621 coupling and tectonic block rotations in the North Island, New Zealand. *Journal of*
622 *Geophysical Research* 109.

623 Wallace, L. M., & Beavan, J. (2006). A large slow slip event on the central Hikurangi
624 subduction interface beneath the Manawatu region, North Island, New Zealand.
625 *Geophysical Research Letters*, 33(11).

626 Wallace, L. M., Reyners, M., Cochran, U., Bannister, S., Barnes, P. M., Berryman, K., et al.
627 (2009). Characterizing the seismogenic zone of a major plate boundary subduction thrust:
628 Hikurangi Margin, New Zealand. *Geochemistry, Geophysics, Geosystems*, 10(10).

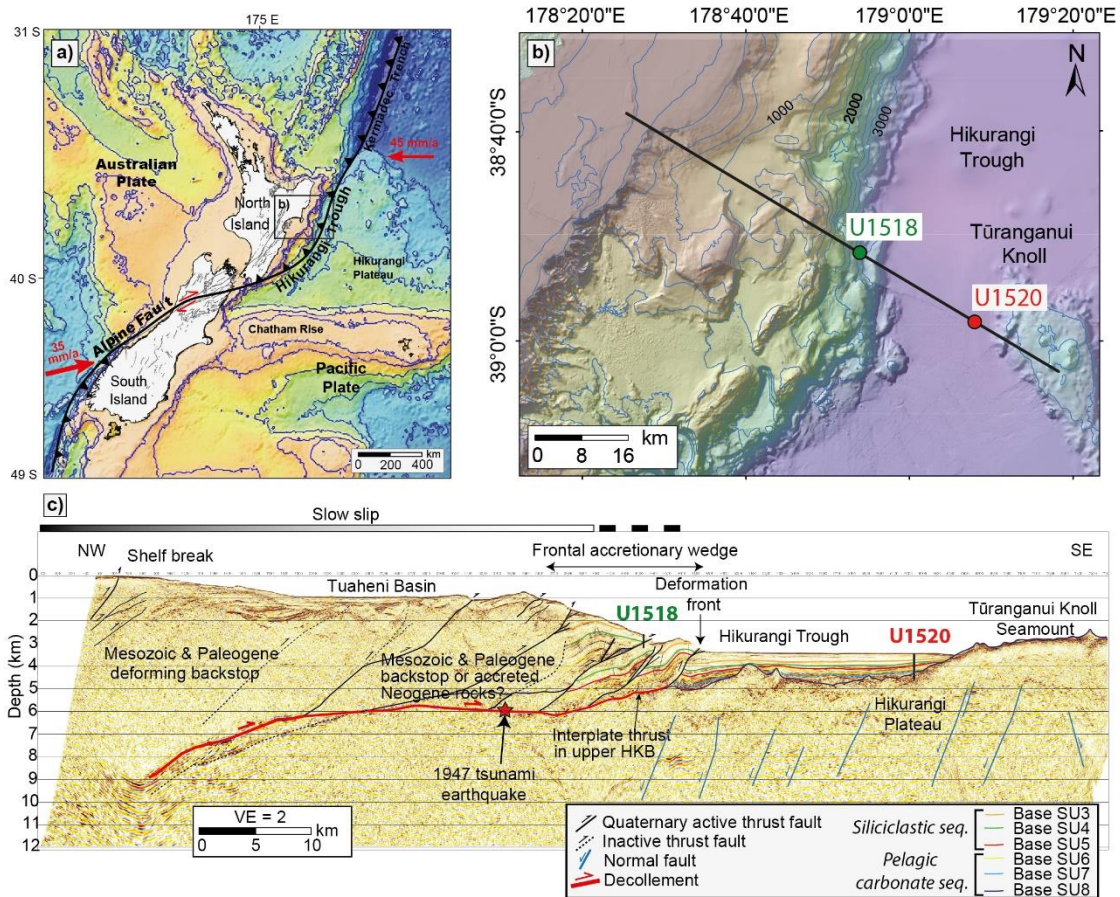
629 Wallace, L. M., & Beavan, J. (2010). Diverse slow slip behavior at the Hikurangi
630 subduction margin, New Zealand. *Journal of Geophysical Research: Solid Earth*, 115(B12).

631 Wallace, L. M., Beavan, J., Bannister, S., Williams, C. (2012). Simultaneous long-term
632 and short-term slow slip events at the Hikurangi subduction margin, New Zealand:
633 Implications for processes that control slow slip event occurrence, duration, and
634 migration. *J. Geophys. Res.* 117, B11402.

635 Wallace, L. M., Webb, S. C., Ito, Y., Mochizuki, K., Hino, R., Henrys, S., et al. (2016).
636 Slow slip near the trench at the Hikurangi subduction zone, New Zealand. *Science*,
637 352(6286), 701-704.

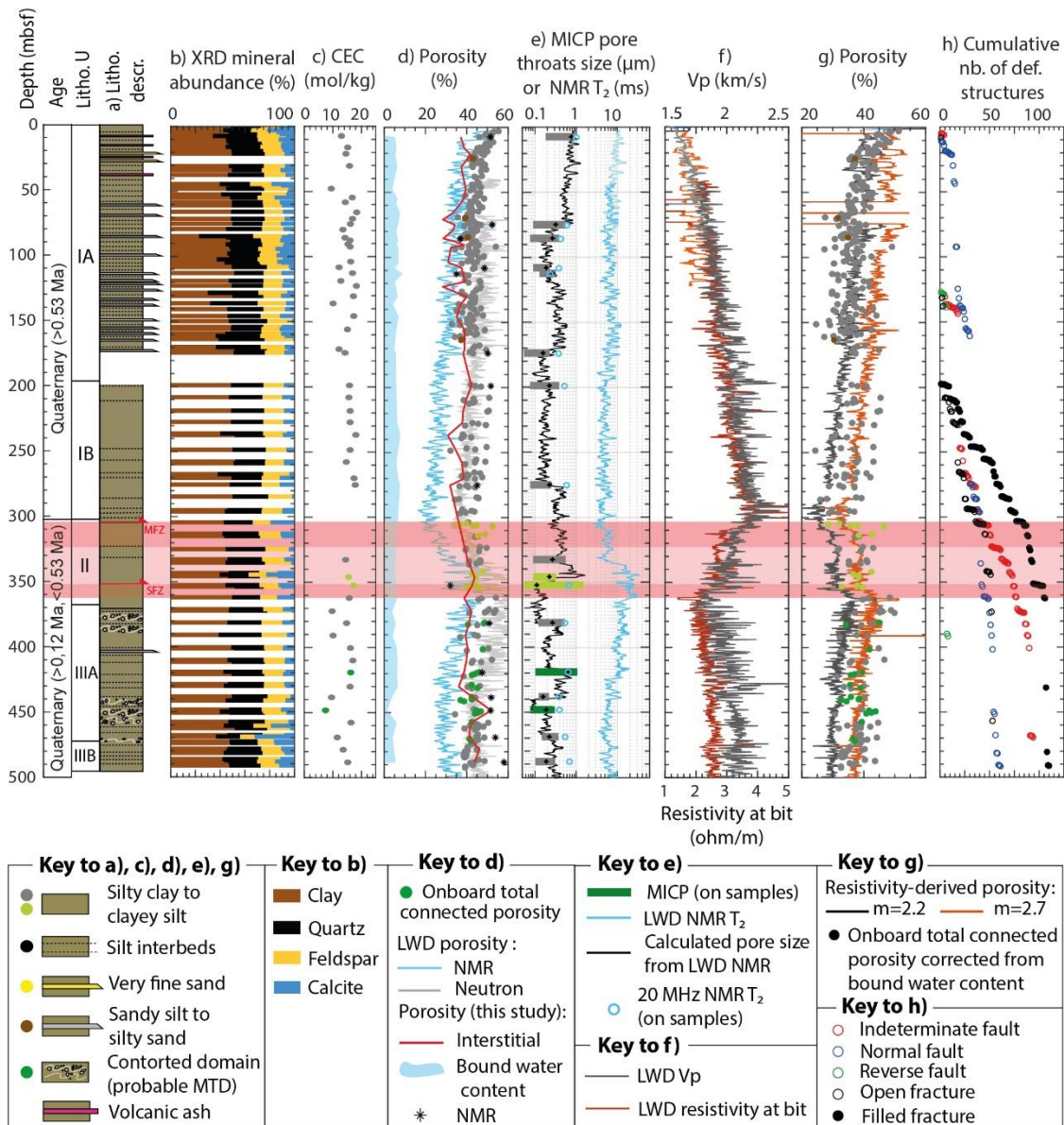
638 Wallace, L.M., Saffer, D.M., Barnes, P.M., Pecher, I.A., Petronotis, K.E., LeVay, L.J.,
639 Bell, R.E., Crundwell, M.P., Engelmann de Oliveira, C.H., Fagereng, A., Fulton, P.M.,
640 Greve, A., Harris, R.N., Hashimoto, Y., Hüpers, A., Ikari, M.J., Ito, Y., Kitajima, H.,
641 Kutterolf, S., Lee, H., Li, X., Luo, M., Malie, P.R., Meneghini, F., Morgan, J.K., Noda,
642 A., Rabinowitz, H.S., Savage, H.M., Shepherd, C.L., Shreedharan, S., Solomon, E.A.,
643 Underwood, M.B., Wang, M., Woodhouse, A.D., Bourlange, S.M., Brunet, M.M.Y.,
644 Cardona, S., Clennell, M.B., Cook, A.E., Dugan, B., Elger, J., Gamboa, D.,
645 Georgiopoulou, A., Han, S., Heeschen, K.U., Hu, G., Kim, G.Y., Koge, H., Machado,
646 K.S., McNamara, D.D., Moore, G.F., Mountjoy, J.J., Nole, M.A., Owari, S., Paganoni,
647 M., Rose, P.S., Screatton, E.J., Shankar, U., Torres, M.E., Wang, X., and Wu, H.-Y.
648 (2019). Expedition 372B/375 methods. In Wallace, L.M., Saffer, D.M., Barnes, P.M.,
649 Pecher, I.A., Petronotis, K.E., LeVay, L.J., and the Expedition 372/375 Scientists,

650 Hikurangi Subduction Margin Coring, Logging, and Observatories. Proceedings of the
651 International Ocean Discovery Program, 372B/375: College Station, TX (International
652 Ocean Discovery Program). <https://doi.org/10.14379/iodp.proc.372B375.102.2019>
653 Wang, K., and Bilek, S.L. (2014). Invited review paper: Fault creep caused by
654 subduction of rough seafloor relief. *Tectonophysics*, v. 610, p. 1–24,
655 <https://doi.org/10.1016/j.tecto.2013.11.024>.



656

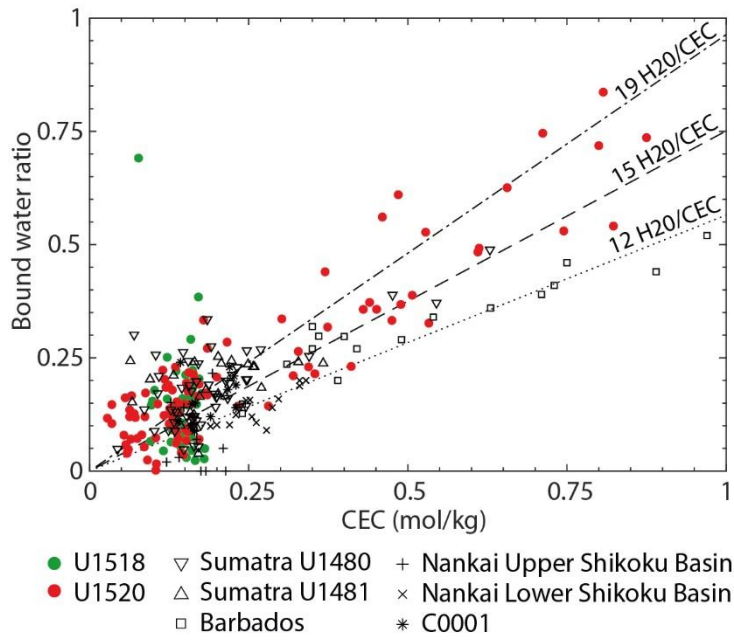
657 Figure 1. a) Tectonic setting of the Hikurangi margin with plate motion indicated by red
 658 arrows. b) bathymetric map of the IODP Expeditions 372/375 study area offshore
 659 Gisborne located on a). The black line represents c) the seismic profile 05CM-04 across
 660 the margin with main seismic reflectors and structures interpreted from the seismic
 661 (Barnes et al., 2020; Fagereng et al., 2019). The red star shows the projected location of
 662 March 1947 tsunami earthquake and VE means vertical exaggeration. a), b) and c) are
 663 modified from Wallace et al., 2019.



664

665 Figure 2. Lithological units, age and description (a) modified after Wallace et al., 2019
 666 mineralogy from onboard XRD (b), cation exchange capacity (c), porosity (d; g), pore
 667 structure (e; MICP bars represent pore throat diameters corresponding to at least 40% of
 668 the maximal mercury injection, the black star corresponds to average pore throats
 669 diameter), (f) LWD resistivity at bit and P-wave velocity (Vp) and deformation
 670 structures (h) at Site U1518. The colors of the data points in c), d), e) and g) and MICP
 671 bars in e) indicates lithology as reported in the first column. The red shaded zone
 672 corresponds to the Pāpaku fault zone with the main fault zone (MFZ from 304 to 322
 673 mbsf) and subsidiary fault zone (SFZ from 351 to 361 mbsf). LWD data at hole
 674 U1518B were shifted from an average value of -12 mbsf to fit core data following

675 Saffer et al., 2019. For e) and f) LWD data, lighter colors correspond to hole U1518A,
676 darker colors to hole U1518B.

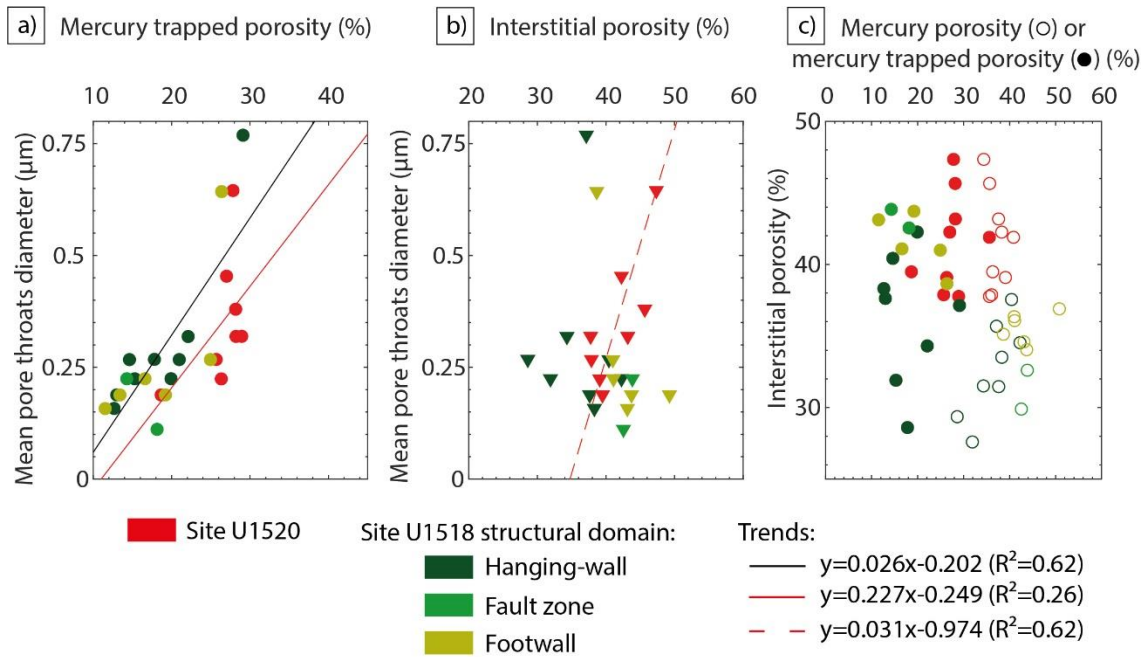


677

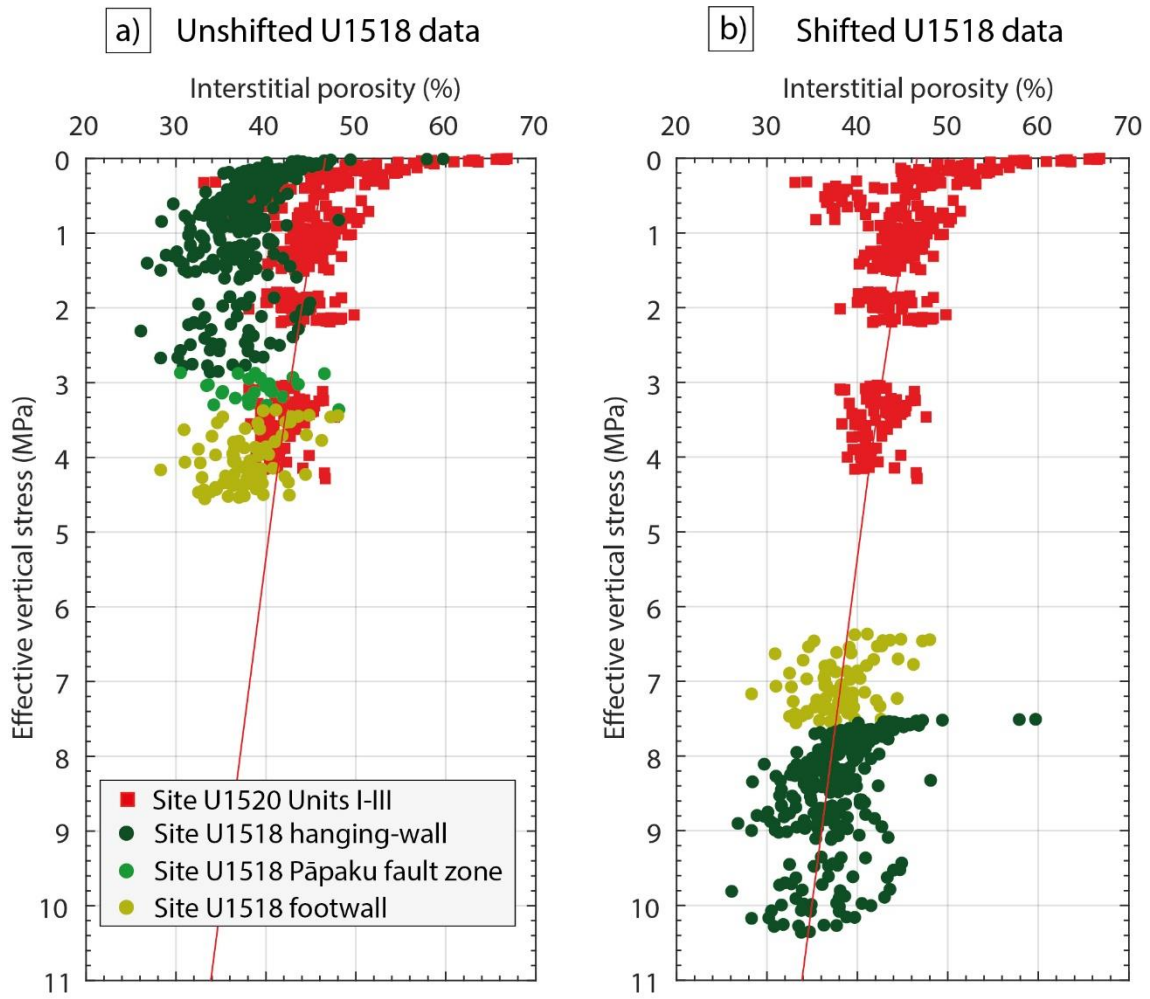
678 Figure 3. Volume of chloride-free fluid per volume of grain (bound water ratio) versus
 679 cation exchange capacity at North Hikurangi margin Sites U1518 and U1520 (after
 680 Dutilleul et al., in press). Theoretical trends are from Henry and Bourlange (2004) and
 681 Conin et al. (2011) and correspond to ideal two (resp. three) water layers smectite
 682 containing 12, 15 (resp. 19) water molecules per cation charge (Henry, 1997). Data for
 683 Sumatra are from Dutilleul et al. (2020), Barbados are from Henry (1997), Nankai
 684 Upper and Lower Shikoku Basin are from Henry and Bourlange (2004) and Site C0001
 685 are from Conin et al. (2011).

686

687 Figure 4. Relations between pore structure and porosity at Site U1518 (green) in the
 688 hanging-wall, the fault zone and the upper footwall and in siliciclastic Units I-III from
 689 reference Site U1520 (red) (after Dutilleul et al., in press). a) Relation between mean
 690 pore throats diameter and mercury trapped porosity. b) Relation between mean pore
 691 throats diameter and interstitial porosity. c) Relation between interstitial porosity and
 692 mercury porosity (open circles) or mercury trapped porosity (circles). Trends were
 693 determined using the least square method.



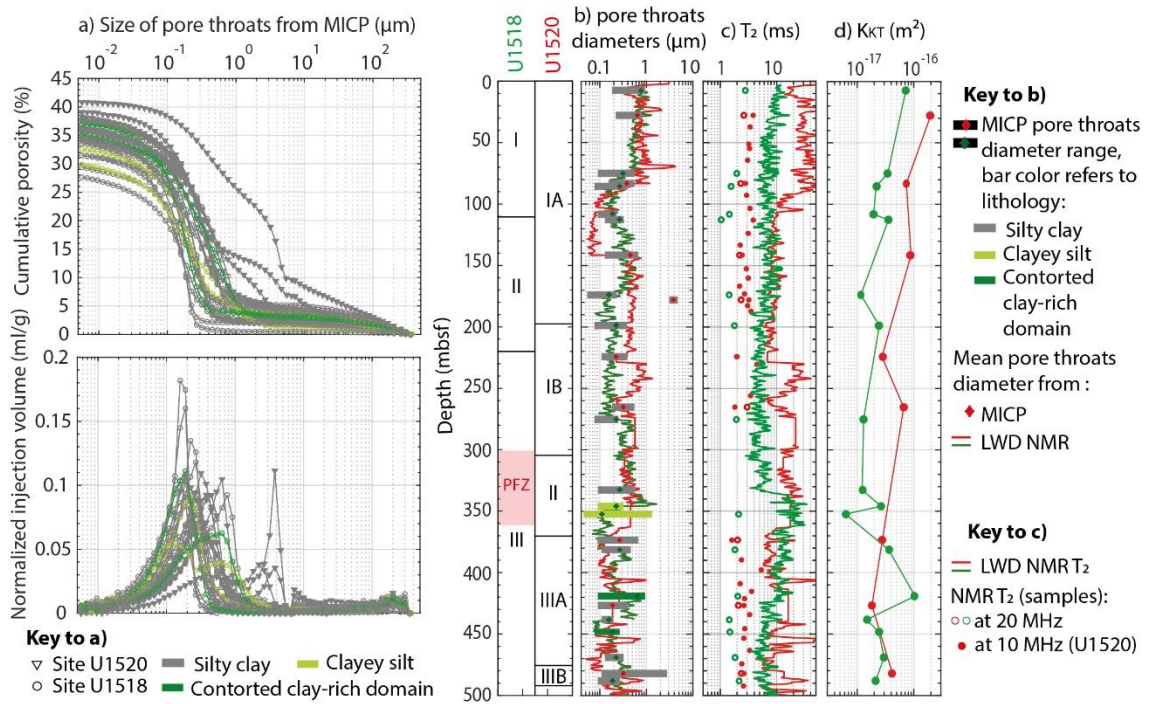
694



695

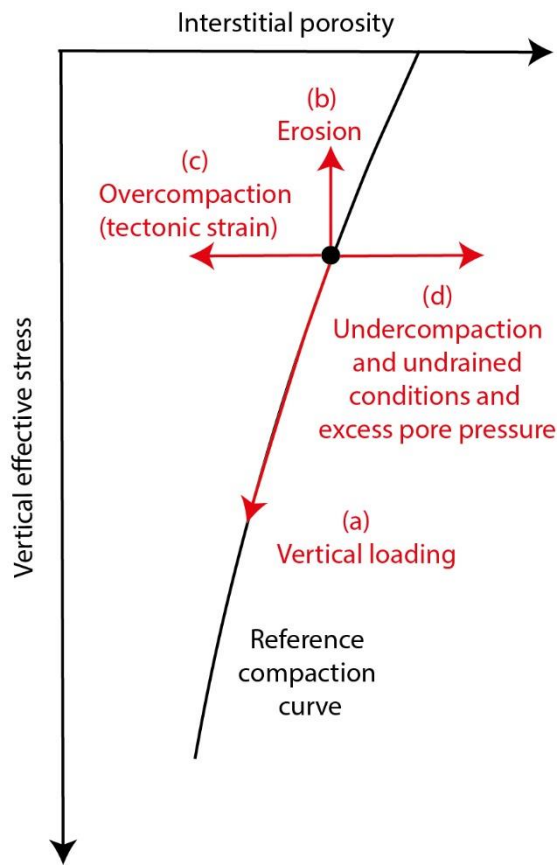
696 Figure 5. a) Comparison of interstitial porosity data at Site U1518 (green) and reference
 697 Site U1520 (red), with reference compaction trend $\phi_i = 46.6e^{-0.029 \sigma_v'} (R^2=0.29)$ (red
 698 line) corresponding to Site U1520 siliciclastic Units I to III, sand-rich and very shallow
 699 unconsolidated samples excluded. b) Vertical effective stress shifts to fit interstitial
 700 porosity data of Pāpaku thrust hanging-wall (dark green, +7.5 MPa or ~830 mbsf) and
 701 footwall (light green, +3.0 MPa or ~330 mbsf) to the reference compaction curve.

702 Figure 6. Comparison of a) MICP pore throats size distribution, b) main pore throats
 703 diameters, c) NMR T_2 , and d) Katz-Thompson permeability K_{KT} of samples from Site
 704 U1518 (green) and Site U1520 (red) siliciclastic Units I-III (Dutilleul et al., in press).
 705 The red PFZ zone corresponds to the Pāpaku fault zone at Site U1518 (~301-361 mbsf).



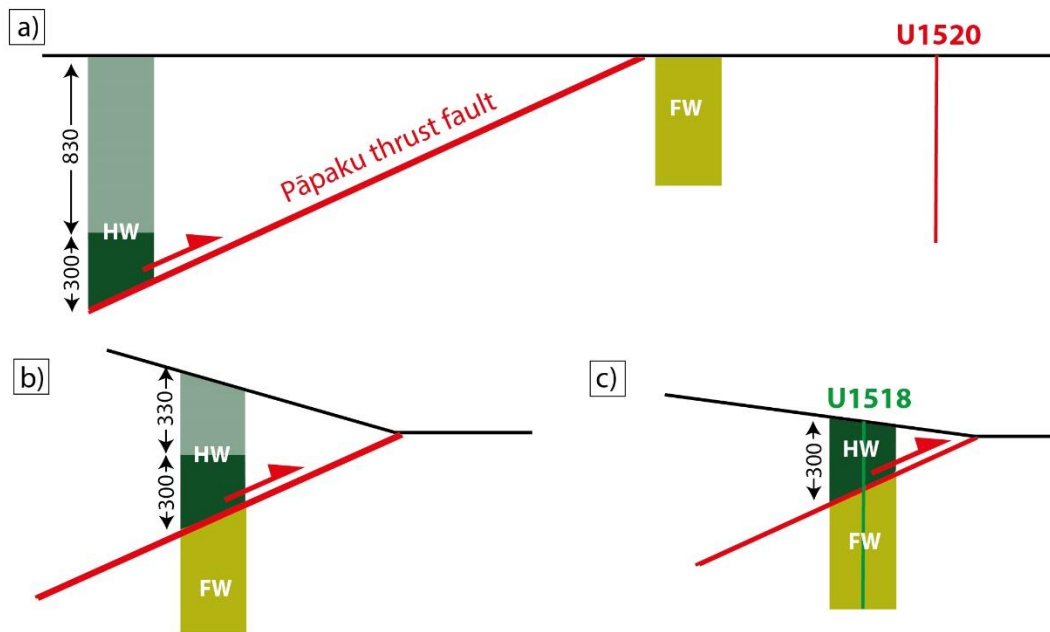
706

707 Figure 7. Tectonic (a, b, c) or hydrologic (d) events affecting interstitial porosity-
708 vertical effective stress pattern.



709

710 Figure 8. Schematic deformation and erosion history at Site U1518, with a) normal
711 consolidation of the hanging-wall (HW) and the footwall (FW) in the entering basin;
712 thrusting of the hanging-wall above the footwall concomitant with ~500 meters of
713 erosion and c) supplementary erosion of ~330 meters of the hanging-wall once it is set
714 above the footwall to finally reach present setting.



715
716

Type of porosity\Zone	Entire sequence	Hanging-wall	Footwall
a) Total connected porosity ϕ_t	$a=44.3$ $b=0.008275$ $R^2=0.00176$	$a=45.83$ $b=0.04986$ $R^2=0.12$	$a=51.34$ $b=0.04073$ $R^2=0.06421$
b) Interstitial porosity ϕ_i	$a=38.25$ $b=0.008782$ $R^2=0.009$	$a=40.59$ $b=0.08071$ $R^2=0.1778$	$a=42.71$ $b=0.02892$ $R^2=0.0204$

717 Table 1. Parameters for the relation $\phi_{i\ or\ t} = ae^{-b\sigma'_v}$ describing the exponential
718 decrease of a) onboard total connected porosity (ϕ_t) and b) interstitial porosity (i.e: ϕ_i)
719 onboard total connected porosity corrected from average bound water content) with
720 increasing effective vertical stress (σ'_v) in the entire sedimentary section, the hanging-
721 wall only or the footwall only at Site U1518. Parameters are determined using the least
722 square method.

Figure1.

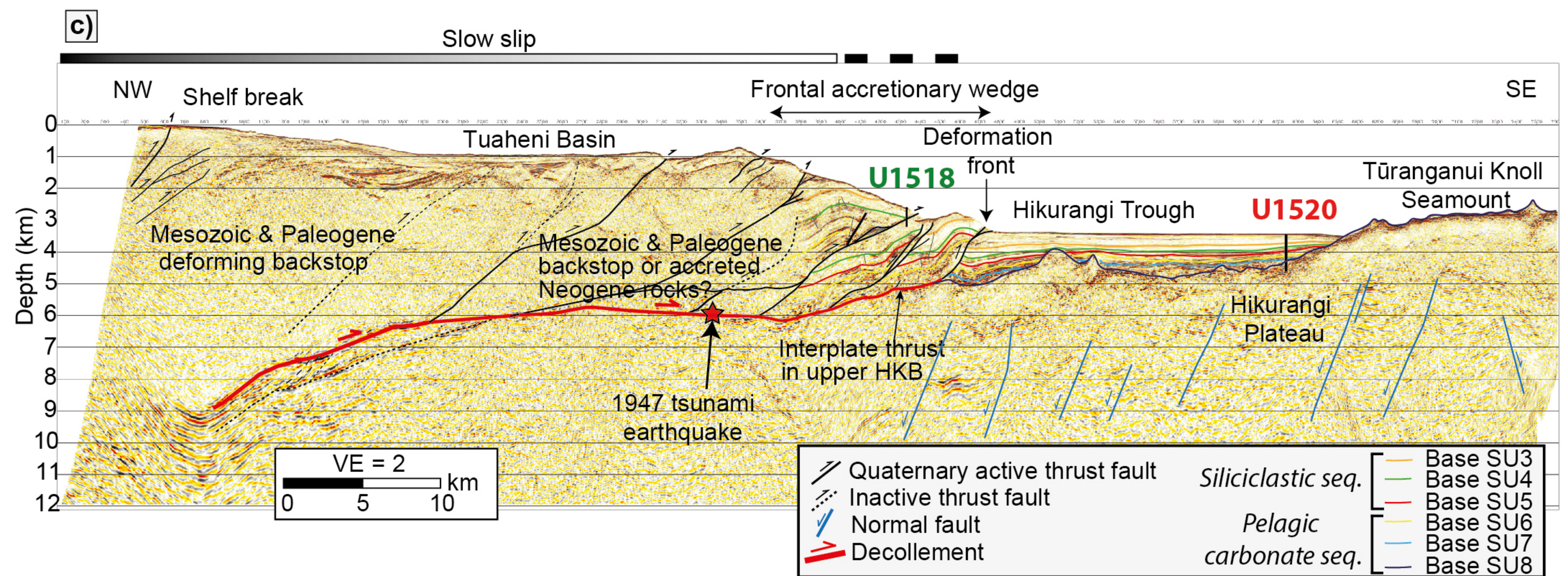
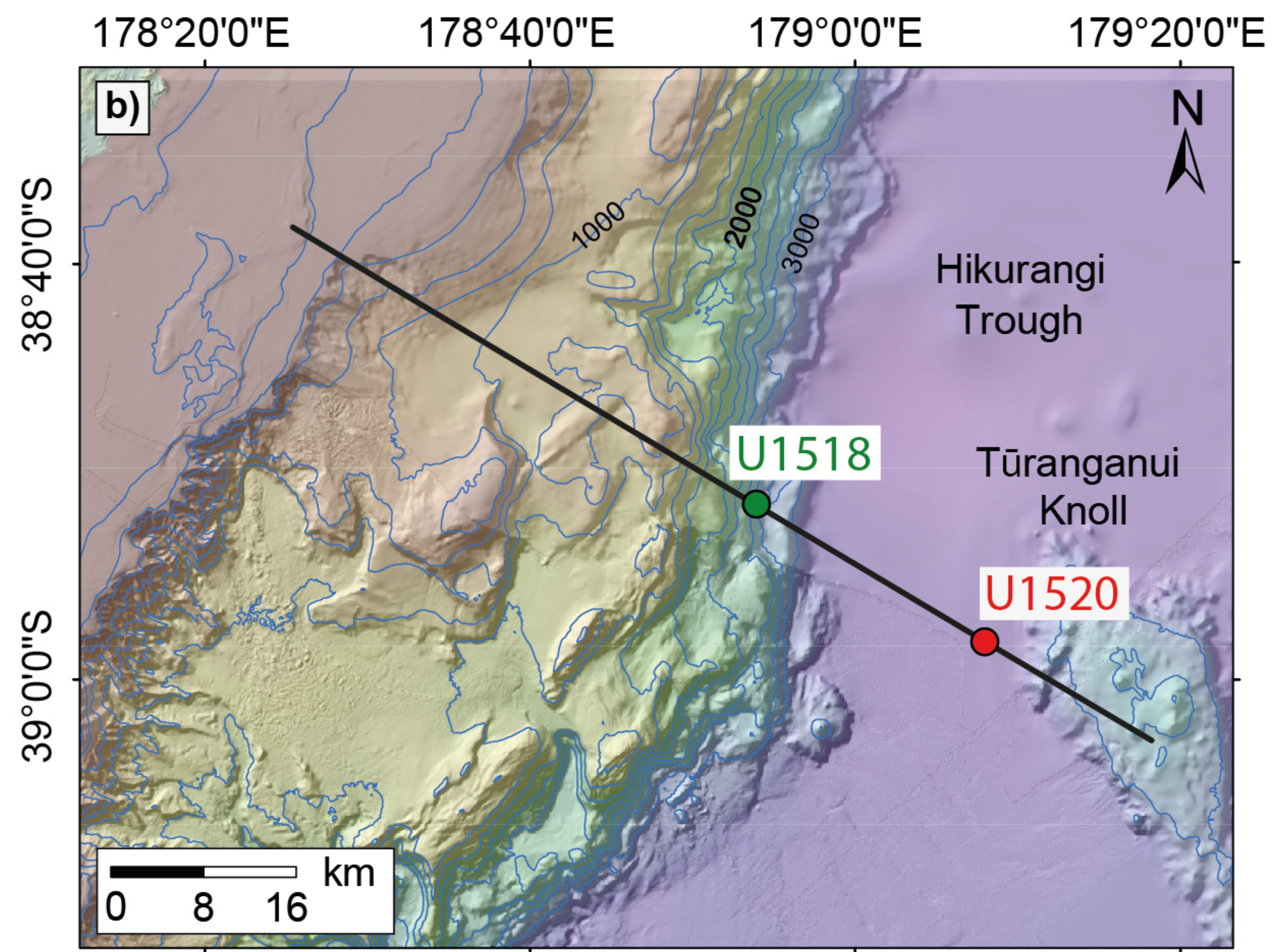
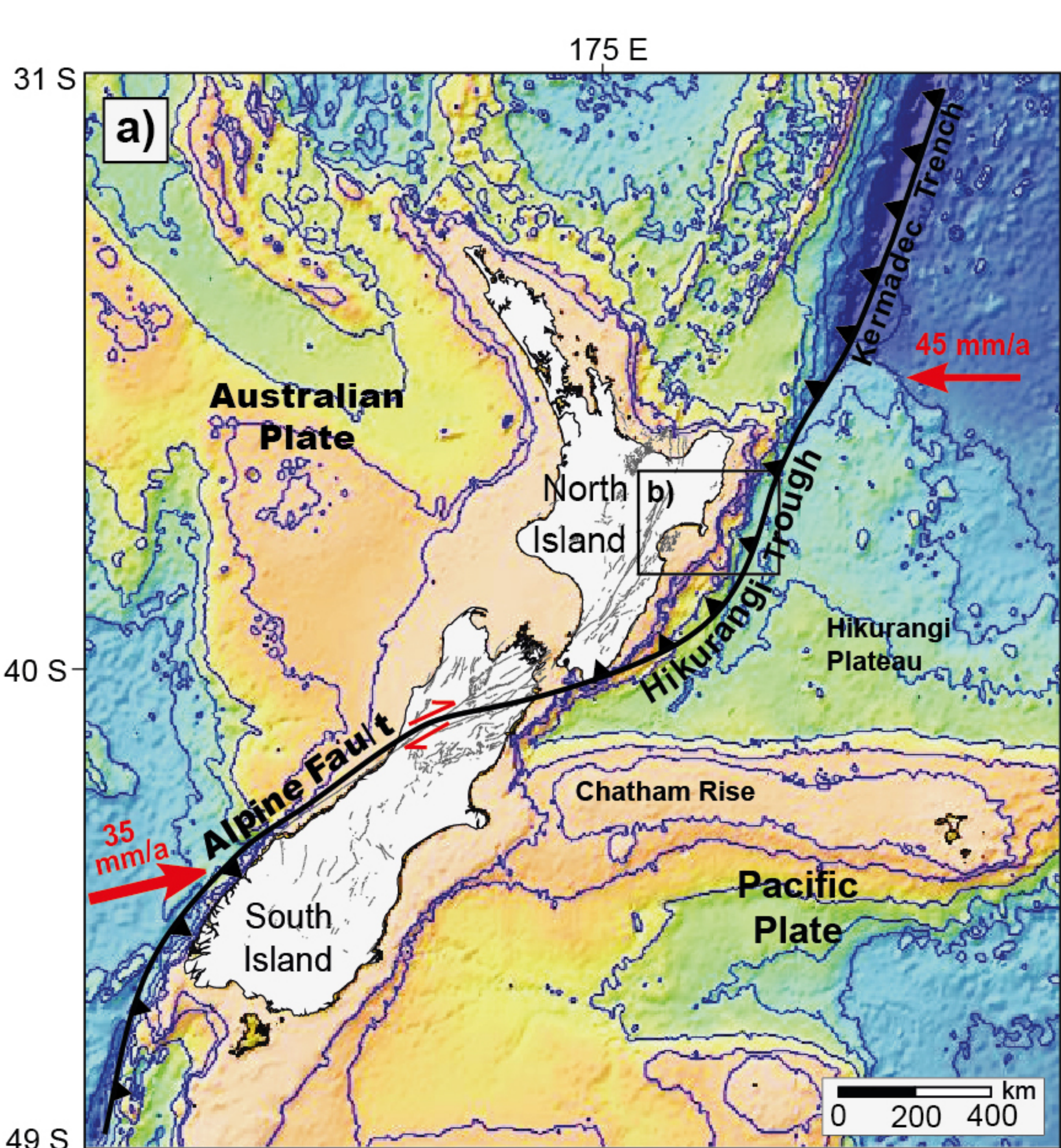


Figure2.

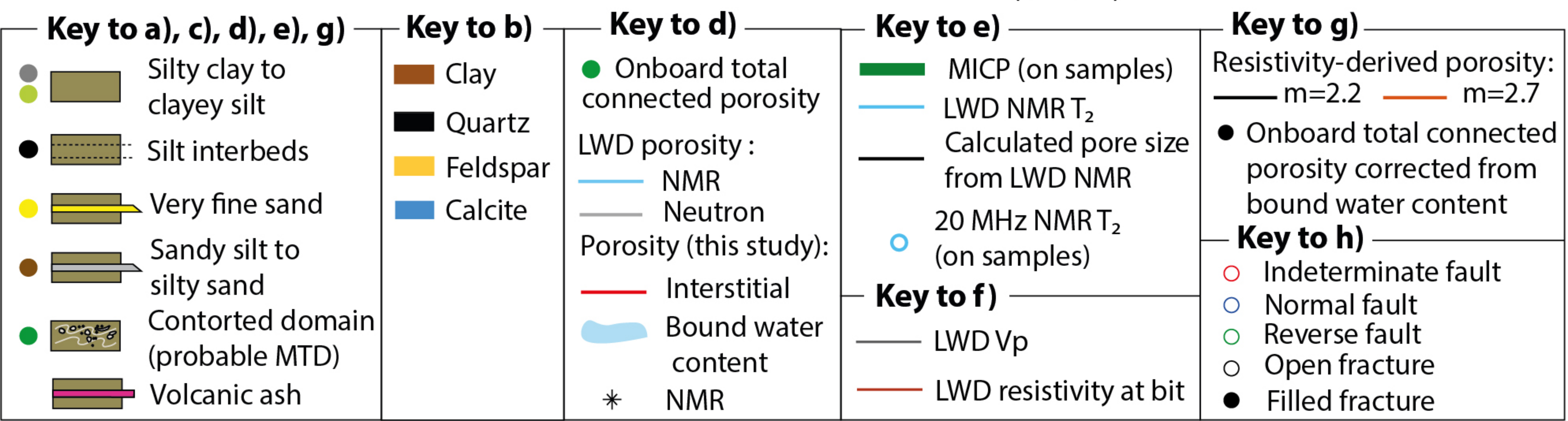
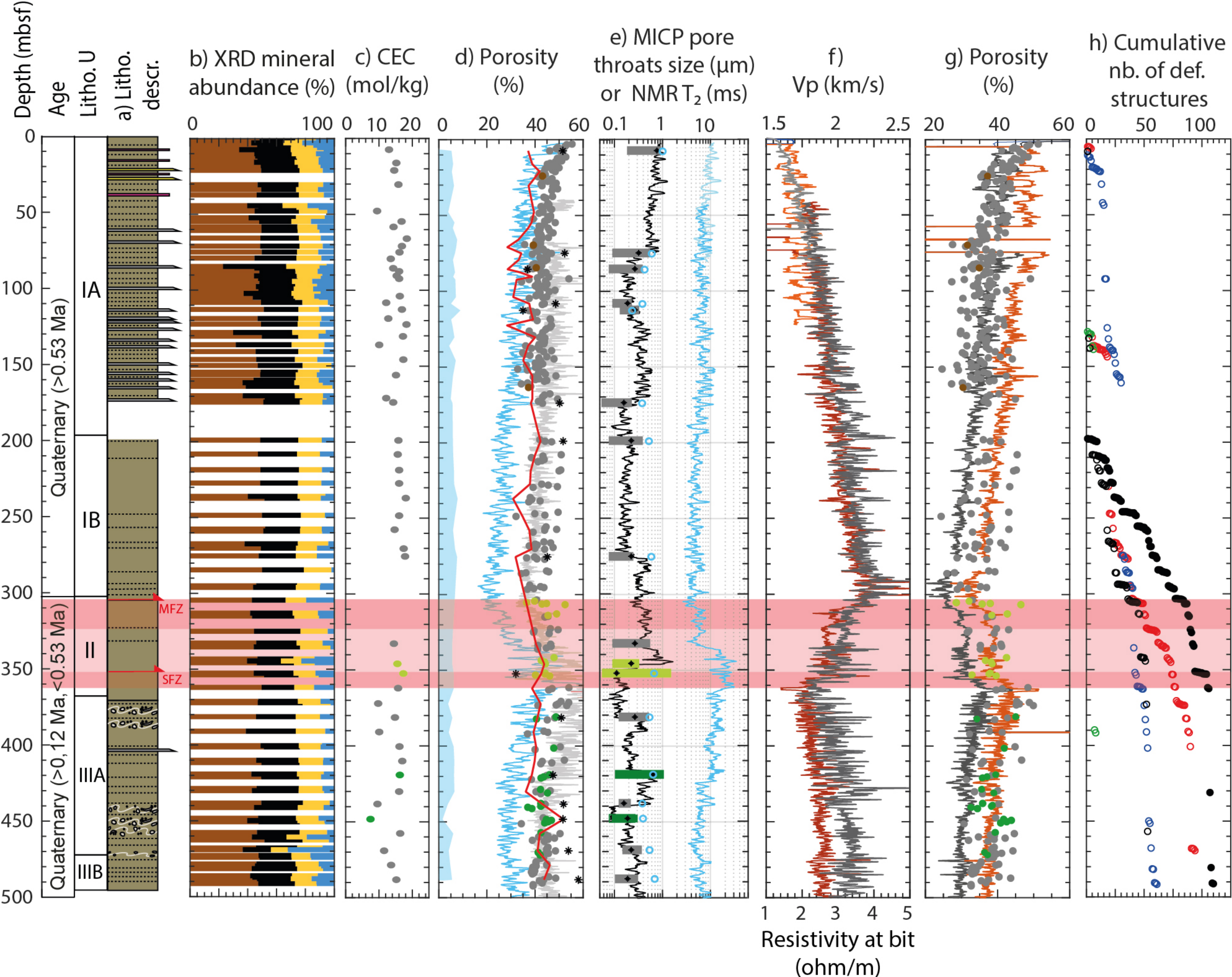
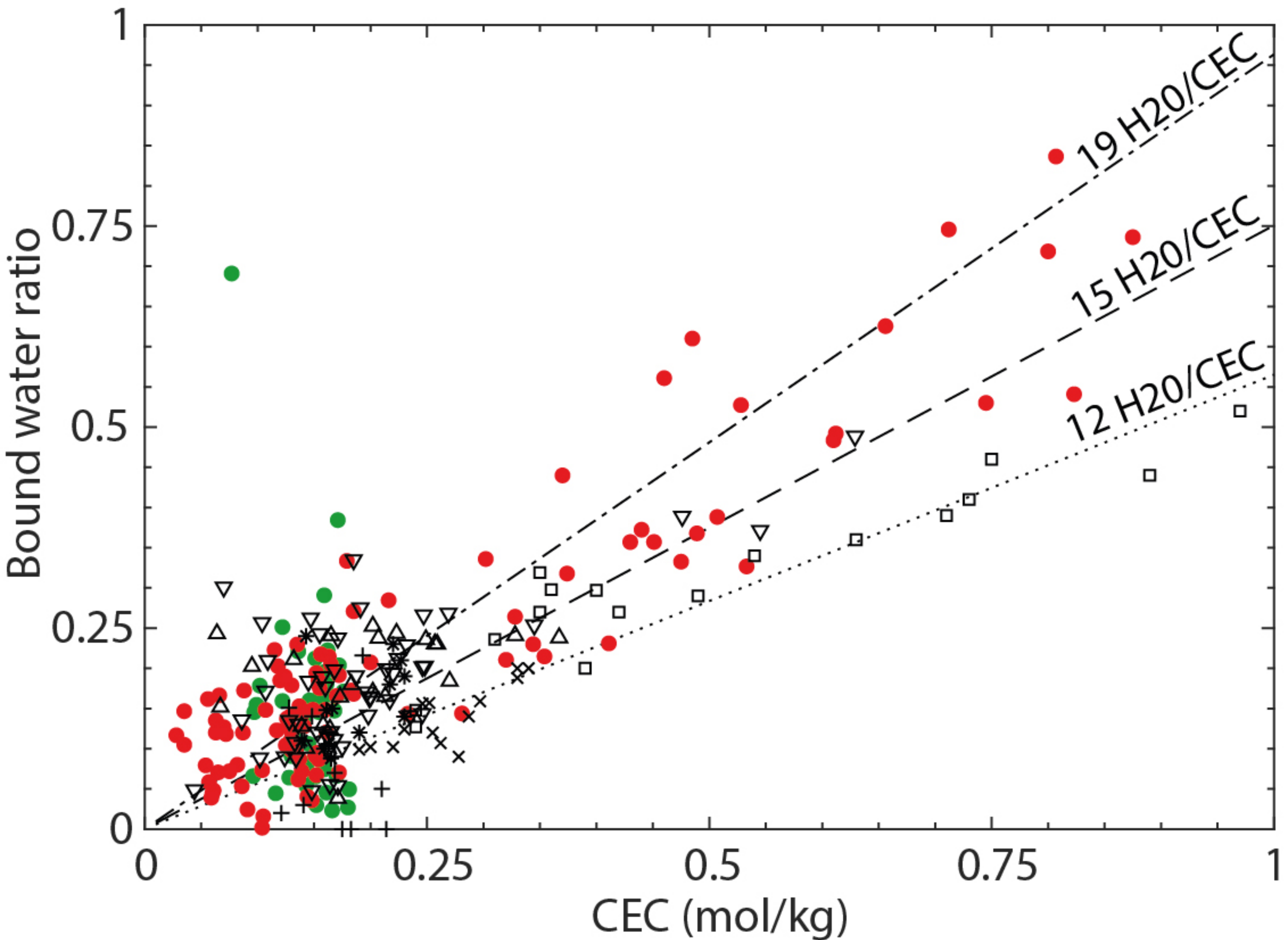


Figure2.



● U1518

▽ Sumatra U1480

+ Nankai Upper Shikoku Basin

● U1520

△ Sumatra U1481

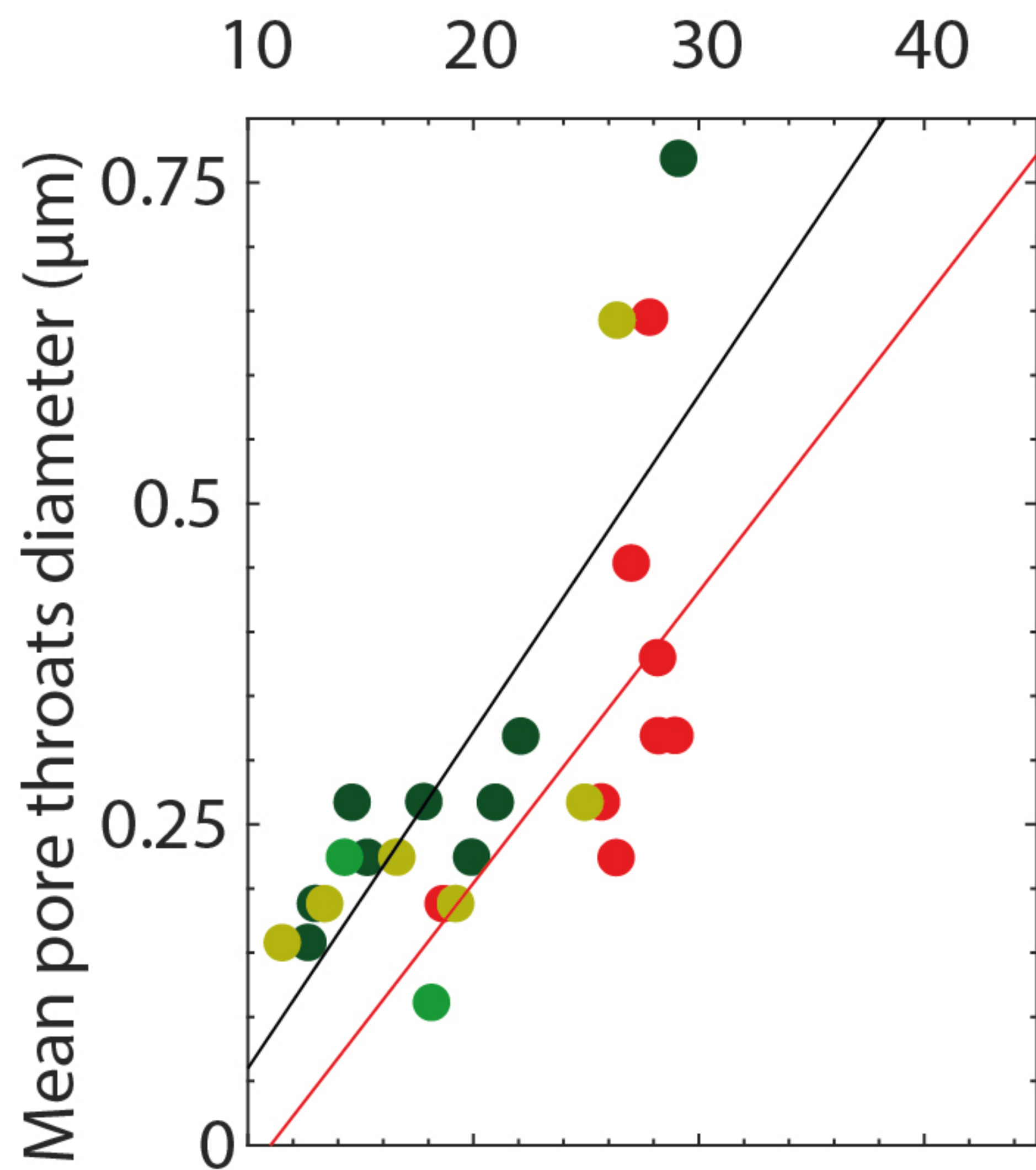
× Nankai Lower Shikoku Basin

□ Barbados

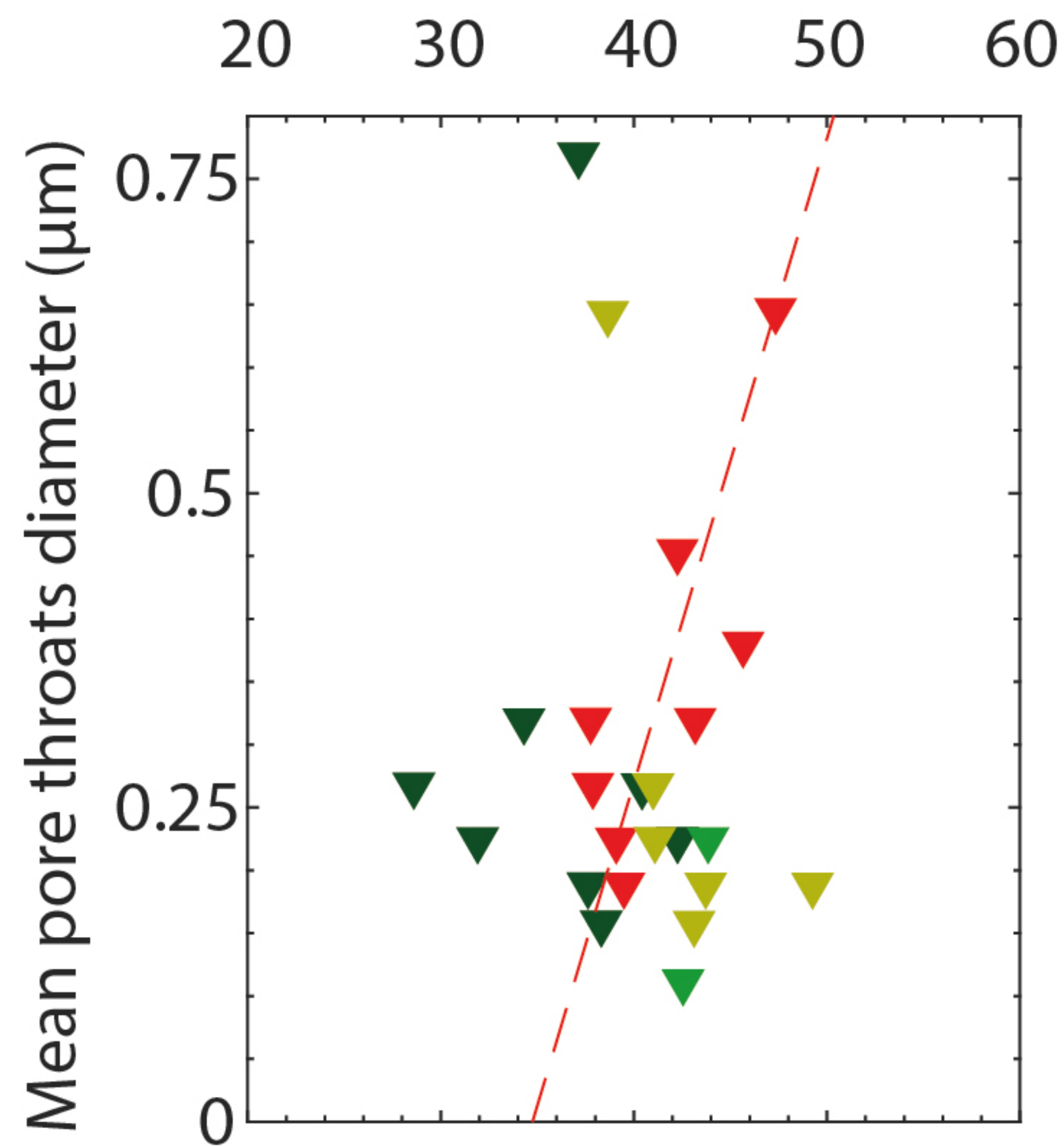
* C0001

Figure4.

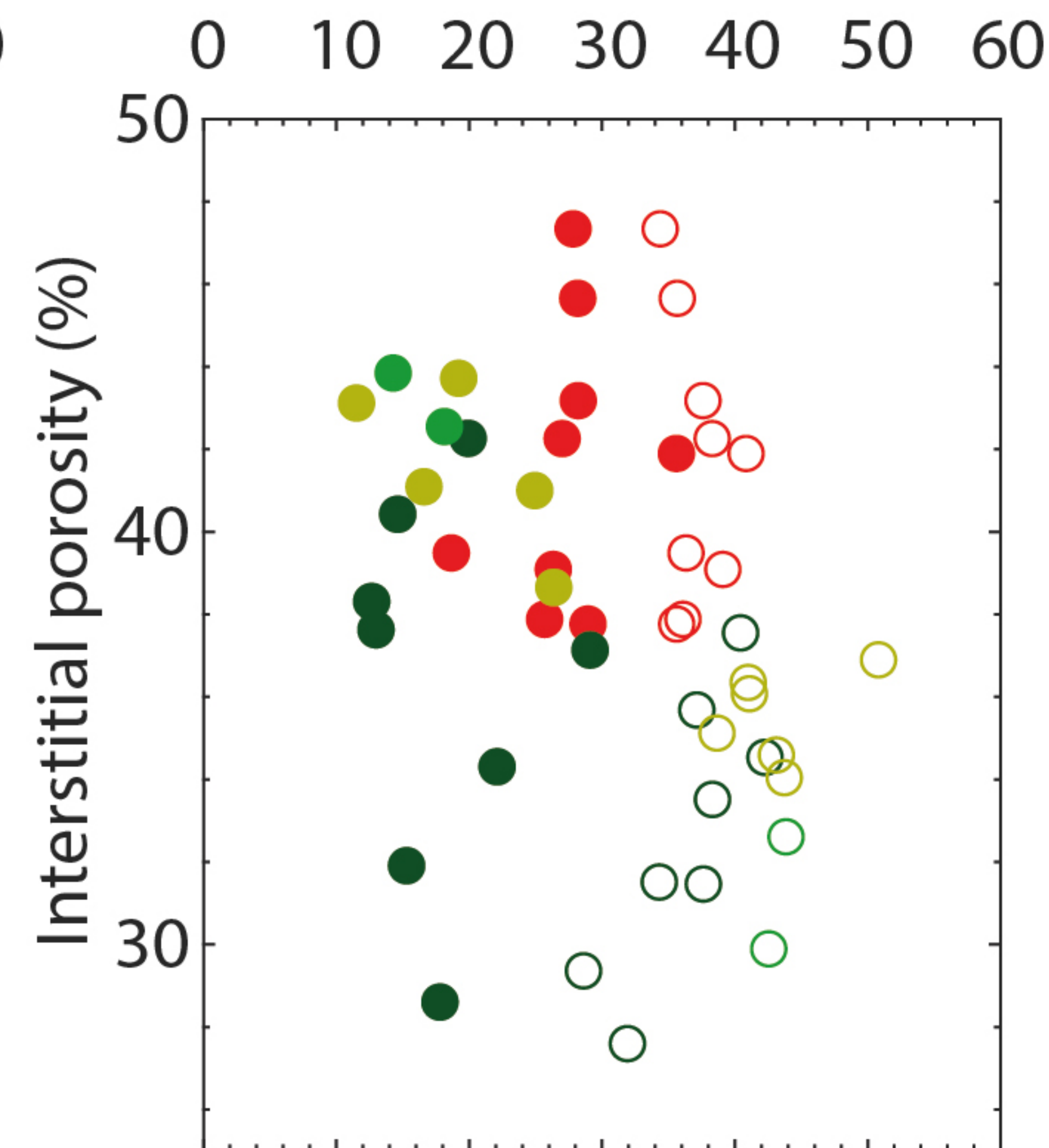
a) Mercury trapped porosity (%)



b) Interstitial porosity (%)



c) Mercury porosity (○) or mercury trapped porosity (●) (%)



■ Site U1520

Site U1518 structural domain:

■ Hanging-wall

■ Fault zone

■ Footwall

Trends:

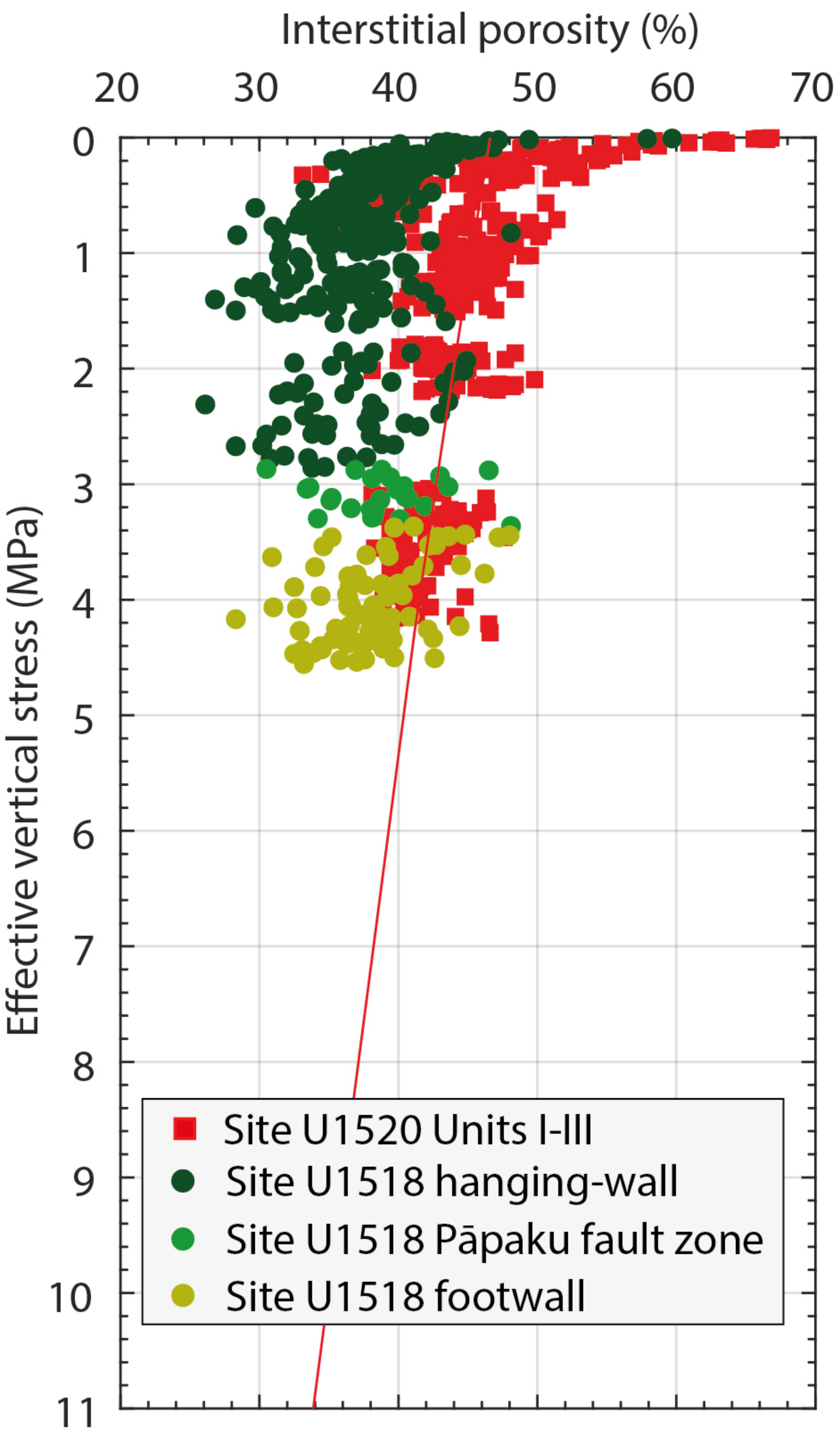
— $y=0.026x-0.202$ ($R^2=0.62$)

— $y=0.227x-0.249$ ($R^2=0.26$)

- - $y=0.031x-0.974$ ($R^2=0.62$)

Figure 5.

a) Unshifted U1518 data



b) Shifted U1518 data

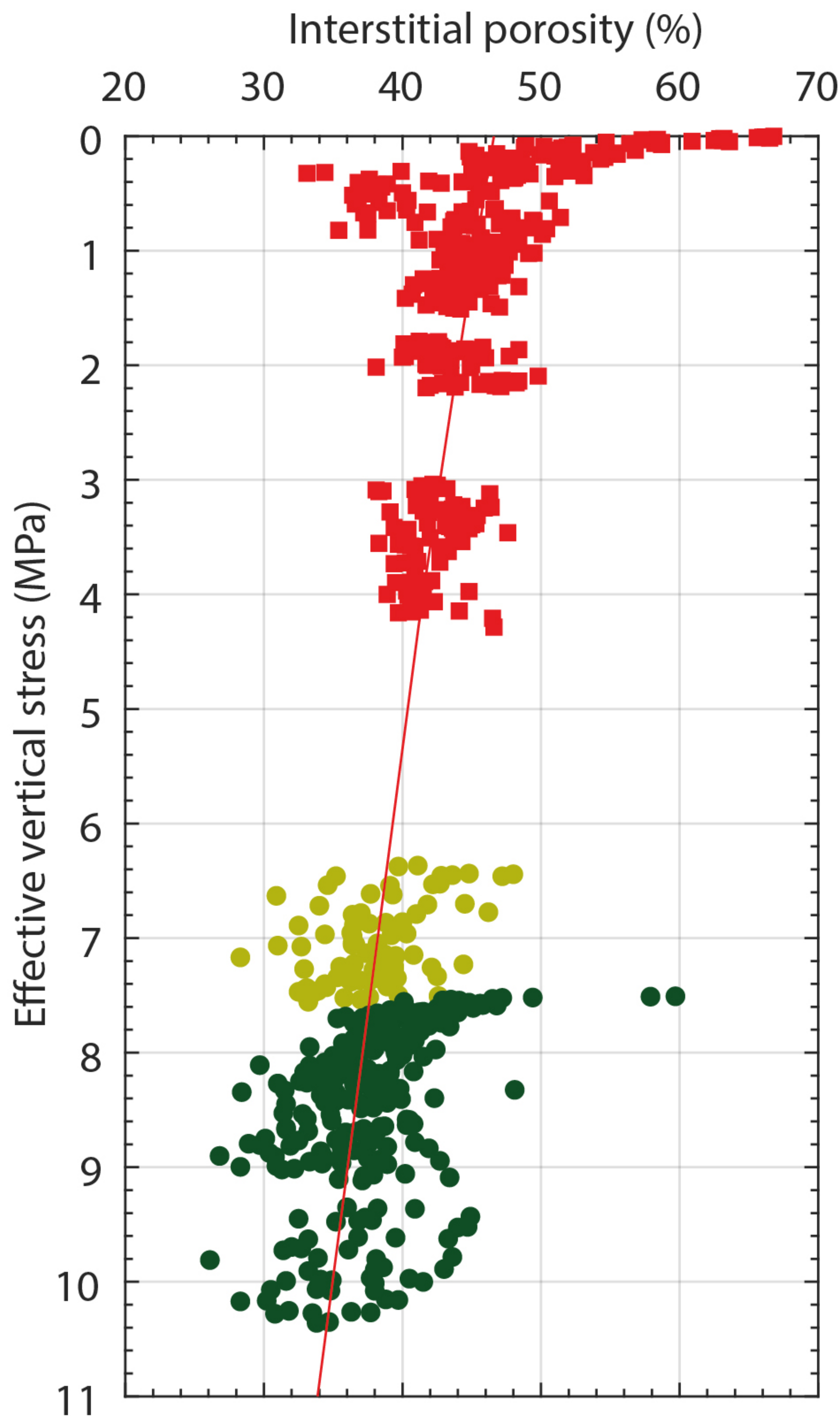


Figure6.

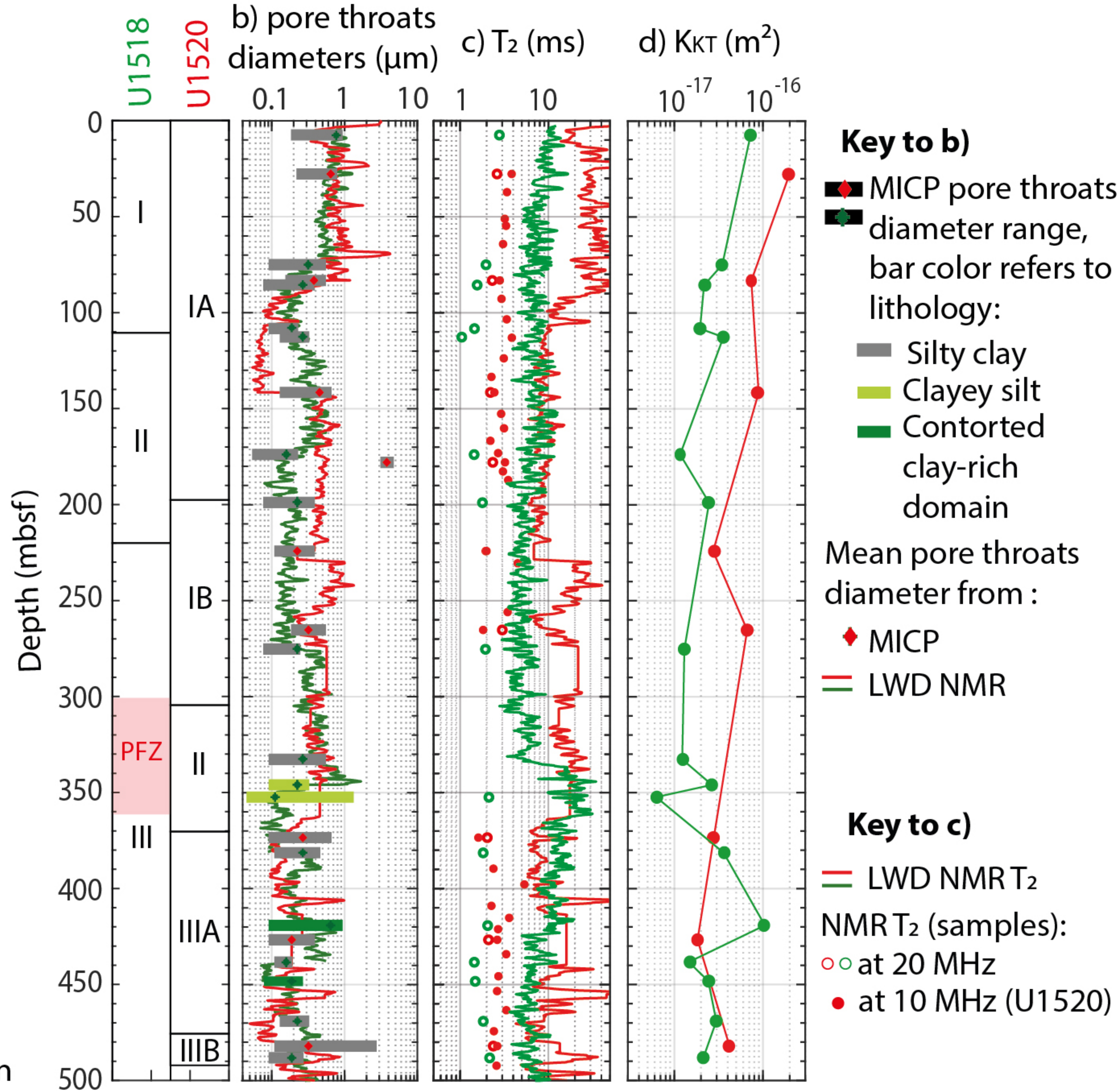
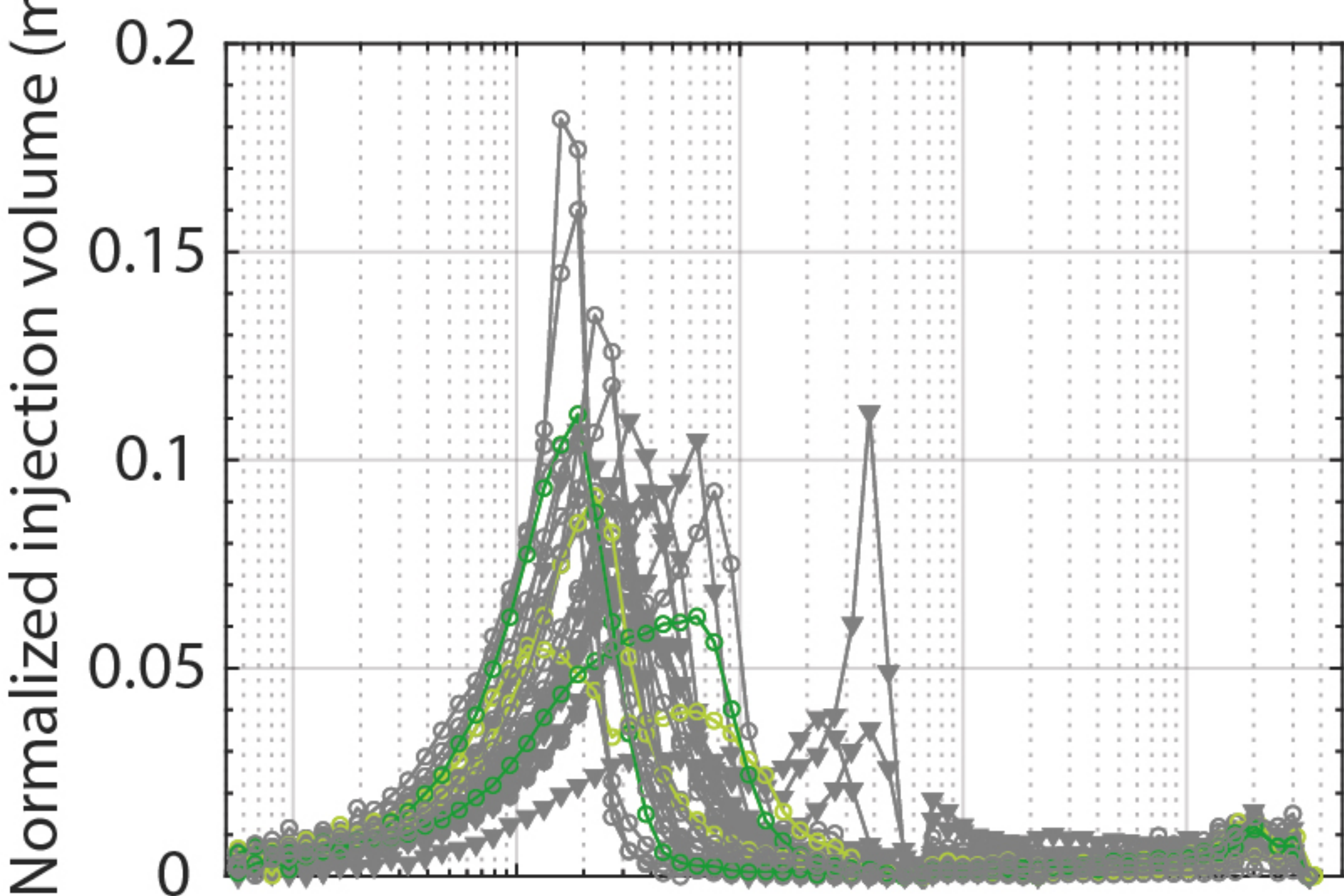
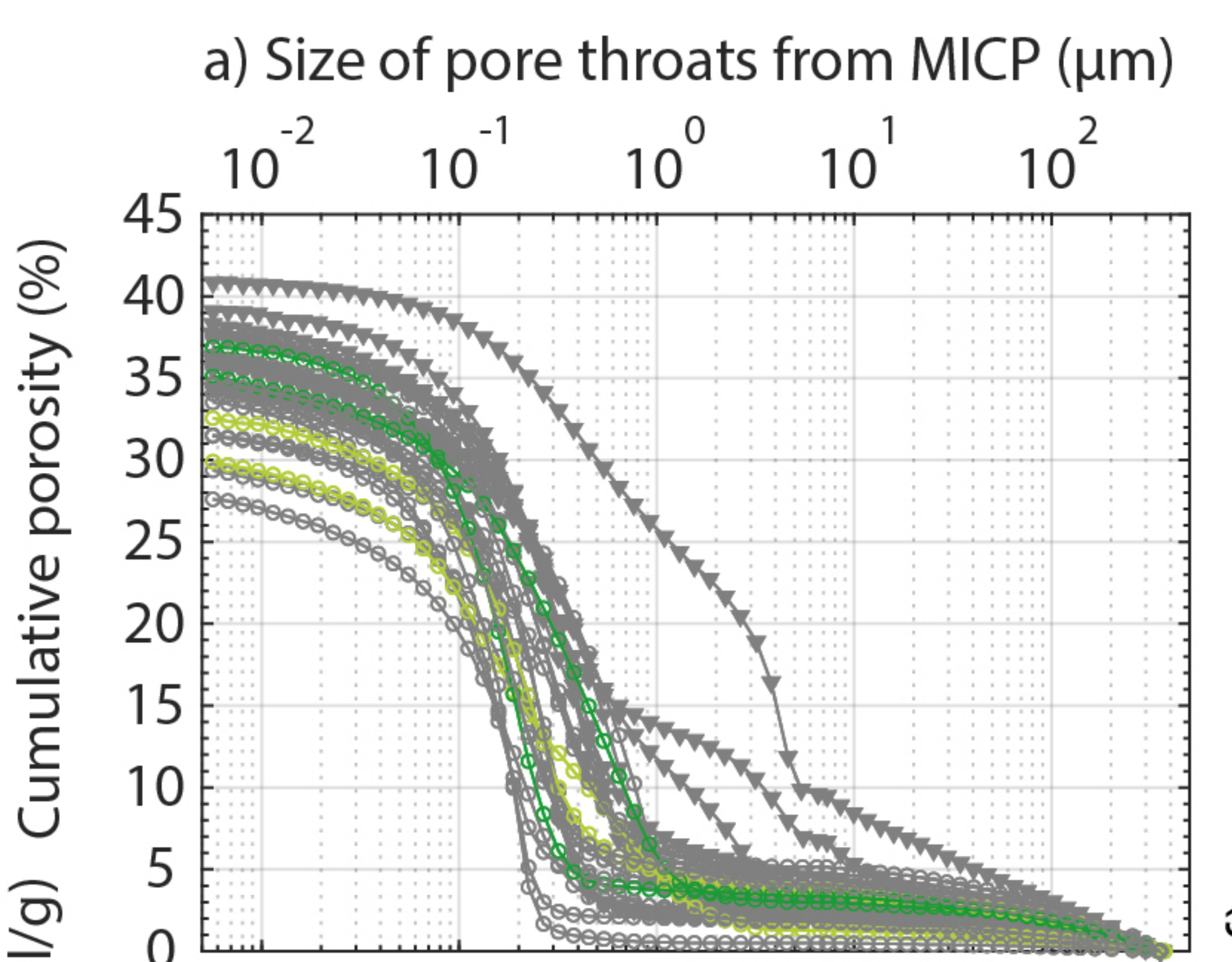


Figure 7.

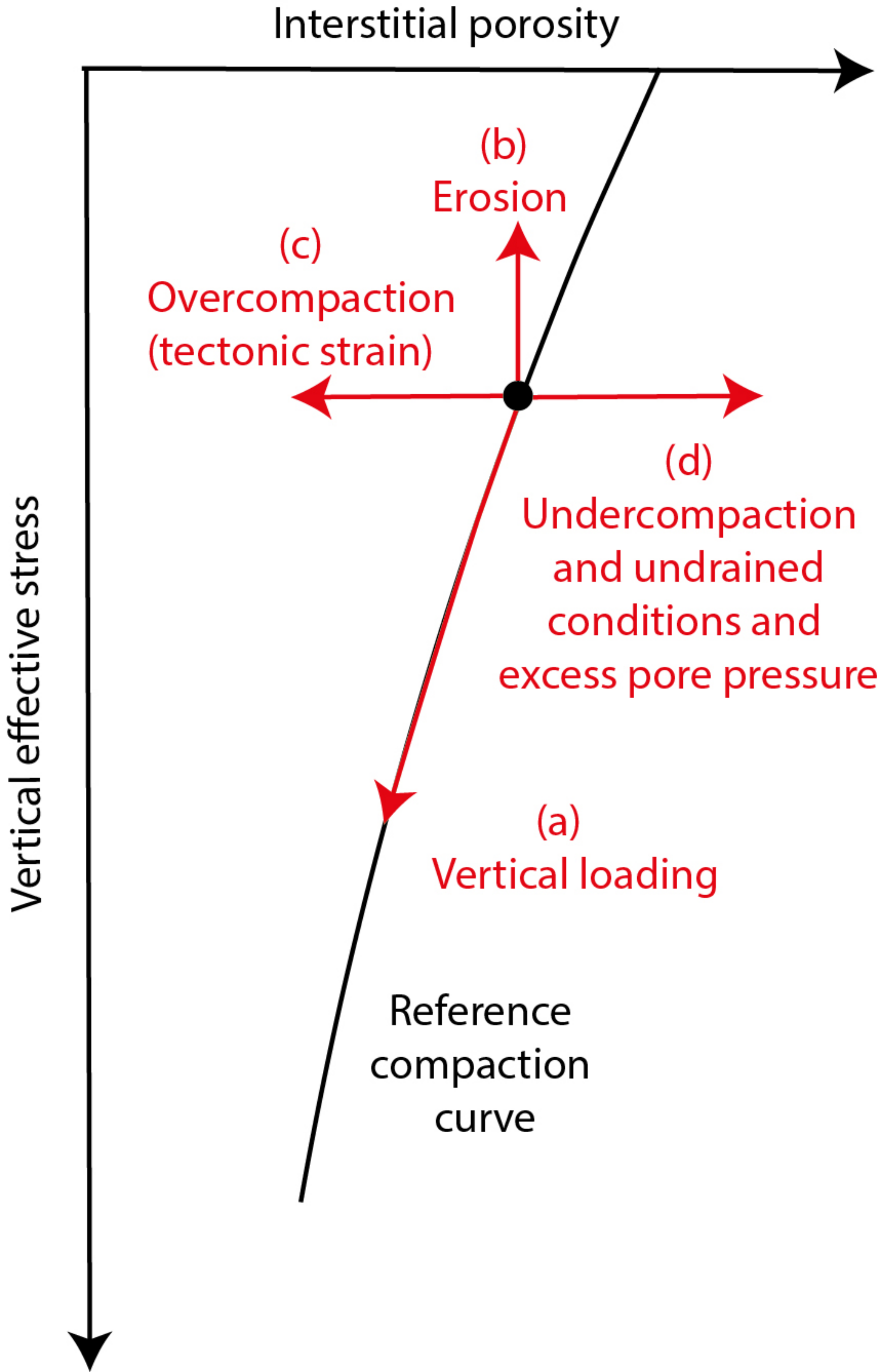


Figure 8.

